J Appl Electrochem (2013) 43:1079–1099
DOI 10.1007/s10800-013-0597-3

RESEARCH ARTICLE

Effect of compression on the performance of a HT-PEM fuel cell

Anja Diedrichs · Maren Rastedt ·
F. Javier Pinar · Peter Wagner

Received: 15 March 2013 / Accepted: 25 July 2013 / Published online: 9 August 2013

Abstract This paper shows by thorough electrochemical investigation that (1) the performances of high-temperature polymer electrolyte fuel cell membrane electrode assemblies of three suppliers are differently affected by compressive forces. (2) Membrane thickness reduction by compressive pressure takes place less than expected. (3) A contact pressure cycling experiment is a useful tool to distinguish the impact of compression on the contact resistances bipolar plate/gas diffusion layer (GDL) and GDL/catalytic layer. A detailed visual insight into the structural effects of compressive forces on membrane and gas diffusion electrode (GDE) is obtained by micro-computed X-ray tomography (μ-CT). μ-CT imaging confirms that membrane and GDEs undergo severe mechanical stress resulting in performance differences. Irreversible GDL deformation behavior and pinhole formation by GDL fiber penetration into the membrane could be observed.

Keywords Fuel cell · HT-PEMFC · PBI · Compression · Micro-computed tomography

Abbreviations

BPP	Bipolar plate
CCU	Cell compression unit
CL	Catalytic layer
CT	Computed tomography
CV	Cyclic voltammetry
DPS	Danish Power Systems
EIS	Electrochemical impedance spectroscopy
GDE	Gas diffusion electrode
GDL	Gas diffusion layer
IV	Current–voltage
LSV	Linear sweep voltammetry
MPL	Microporous layer
HT-PEM	High-temperature polymer electrolyte membrane
MEA	Membrane electrode assembly
PBI	Polybenzimidazole
PEMFC	Polymer electrolyte membrane fuel cell
PVDF	Polyvinylidene fluoride
μ-CT	Micro-computed tomography
SEM	Scanning electron microscopy

1 Introduction

A polymer electrolyte membrane fuel cell (PEMFC) is a very promising power source due to its high efficiency and near-zero emission. Because of its beneficial power-to-weight ratio and fast startup time due to low operating temperature, the PEMFC can be utilized in a wide range of applications like stationary, transportation, portable, and micro-fuel cell applications. However, the temperature level of the low-temperature PEMFC has some major disadvantages which have led to the development of the high-temperature (HT)-PEMFC. The disadvantage of a higher operating temperature is the acceleration of degradation effects. Therefore, long-term stability is still an issue for HT-PEMFCs. The degradation effects and mechanisms are not fully understood yet.

A HT membrane electrode assembly (MEA) is a highly complex structure of different materials. During operation

---

A. Diedrichs · M. Rastedt · F. J. Pinar · P. Wagner (✉)
NEXT ENERGY, EWE Research Centre for Energy Technology
at the Carl von Ossietzky University,
Carl-von-Ossietzky Str. 15, 26129 Oldenburg, Germany
e-mail: peter.wagner@next-energy.de

of fuel cells different types of failures can be observed as summarized in Table 1 [1–10]. All MEA components are involved, which are the gas diffusion (GDL) and the catalyst layers (CL) as well as the membrane. There are several possible causes for failures and each of them contributes to the overall fuel cell performance loss. Some of the degradation effects also interact with each other. For example, carbon corrosion decreases the electrical conductivity in the gas diffusion electrode (GDE) [11]. The hydrophobicity in the electrode is also changed by carbon corrosion which then causes reactant deficiency in the end [1, 11]. Moreover, carbon corrosion also leads to catalyst particle detachment and, therefore, to a loss in catalytic activity.

In order to get a chance to identify the different degradation causes and to separate the contribution of each single effect from the total degradation, one basic requirement is to have control over the compression at all times. Compression is one of the key parameters for fundamental degradation investigations because it has an impact on many MEA properties as summarized in Table 2 [7, 12–15]. For example, high compressive forces should improve the contact between the different MEA components which results in a decrease of the ohmic resistance [16]. A compression change might also affect the distribution of the electrolyte in the CLs which may lead to an enhanced three-phase reaction zone or to electrode flooding. The applied compression should also influence the thickness of the individual layers because these are not stiff. A membrane thickness reduction should decrease the ionic conductivity resistance because the pathway length for the protons gets shorter. On the other hand, a thinner membrane will also shorten the pathway length for gas species crossover and for electrons. A GDL thickness reduction should have an effect on the GDL porosity and, therefore, the access for the reactant gases might be changed. Compression forces could also cause material modifications or real damages which can be analyzed with imaging techniques like scanning electron spectroscopy or, in this paper, with micro-computed X-ray tomography (μ-CT).

μ-CT is a well-known method to investigate samples in three dimensions without destruction or pretreatment. Optical microscopes or scanning electron microscopy (SEM) only allow two-dimensional surface investigation of samples. Therefore, only a limited access to underlying structures is possible, e.g., with focused ion beam ablation. In addition, such an ablation process destroys the sample surface. Another method is slicing samples with a very fine slice dimensions but such an investigation is also coupled with losses of information [17]. Such obstacles can be overcome by applying X-ray CT or synchrotron radiography [18]. The latter requires expensive beam times at large research centers like BESSY II in Berlin within high-energy particle collision experiments. Such beam time is only available during rather short periods within a year and rather expensive. Instead, the imaging technique μ-CT can be achieved with new instruments now available for operation in the standard laboratories.

The understanding of the importance of compression control by the authors has led to first experiments on that topic and the results were recently published [7]. The main goal of this paper is to provide an update with new experimental results for HT-PEMFC operation at defined contact pressures and to couple these results to three-dimensional images obtained with a μ-CT. The MEAs were thoroughly electrochemically characterized by current–voltage curves (IV), electrochemical impedance spectroscopy (EIS), cyclic voltammetry (CV), and linear sweep voltammetry (LSV). In addition, the GDL material and

Table 1 Some observed failures and possible causes for high-temperature MEAs

Observed failures	Possible causes
Conductivity loss	Phosphoric acid leaching (cold start [→ dilution with liquid water])
	Carbon support corrosion (start/stop, load profile, reactant starvation)
	Contact change between MEA components (compression)
	Contact change between MEA and flow field (compression)
Catalytic activity loss	Catalyst particle dissolution (hot phosphoric acid, load profile)
	Catalyst particle agglomeration (load profile)
	Catalyst particle detachment (carbon support corrosion)
	Reactant contamination (e.g., CO, SO_2, H_2S,…)
Membrane defect	Dissolution/pinhole (radical attack)
	Fracture (thermal cycle, pressure difference, compression)
	Contamination (e.g., metal ions from stack components)
Reactant deficiency	Flow field design
	Phosphoric acid flooding of electrode due to hydrophobicity change (modification of carbon support functional groups, carbon support corrosion, ionomer dissolution)

Table 2 Role of compression for high-temperature MEA

Possible effect on	Possible consequence for
GDL porosity	Reactant supply
Membrane thickness	Ionic resistance Reactant crossover Internal short circuit
H_3PO_4 penetration into catalytic layer	Three-phase reaction zone Flooding (→ reactant supply)
Electrical contact	Electrical resistance
Material integrity	Physical modifications and damages

MEA samples were investigated with µ-CT. Therefore, this paper provides a much better insight into the effects of compression on HT-PEMFCs. The influencing effects on single MEA components can be identified by applying a combination of these different characterization methods.

2 Experimental set-up

2.1 Fuel cell testing

2.1.1 Membrane electrode assemblies

For some of the measurements reported here, Celtec®-P2100 MEAs (BASF Fuel Cell, Germany) with an active area of 20.25 cm^2 were used. The MEAs consist of a polymer gel membrane with polybenzimidazole (PBI) and phosphoric acid. The acid content is about 95 wt% which accounts for 70 phosphoric acid molecules per PBI repeat unit [19]. The GDL is a woven carbon cloth with a thickness of 400 µm. Information about further specifications can be found here [20].

A second type of HT-MEA has been provided by FuMA-Tech GmbH (Germany) which has a nominal active surface area of 25 cm^2. The real active surface area is proprietary data and cannot be given here. The polymer in this type of MEA is AB-PBI. Whereas the Celtec®-P2100 MEA employs woven carbon cloth as primary GDL material, the second type of MEA utilizes carbon paper. Further details to the FuMA-Tech–MEA and the materials involved are proprietary information.

A third type of HT-MEA has been provided by Danish Power Systems (DPS, Denmark) with a nominal active surface area of 25 cm^2. The real active area is also proprietary data. This type of MEA uses *m*-PBI as polymer and carbon paper as GDL material. The acid content of this type of MEA is ~8–9 H_3PO_4 molecules per repeat unit of PBI. Further information cannot be given due to proprietary issues.

2.1.2 Cell compression unit and fuel cell test station

A commercially available cell compression unit (CCU) was utilized for these experiments (Pragma Industries, France). The system allows the compression force transmission from a piston directly on the active surface area of the MEA. A displacement sensor on the unit allows recording all thickness changes during the experiments. The system can be operated in either "constant contact pressure" or "constant displacement" mode. The data presented here have been recorded at constant contact pressure mode. The applicable nominal contact pressure range to MEAs varies between 0.2 and 2.5 MPa. A lower contact pressure is generally possible but might result in gas leakages. The effective pressure by a MEA fixture within a compression unit that is applied on a MEA depends on the flow field geometry where the real contact area between bipolar plates (BPPs) and GDLs is only determined by the land and channel dimensions. It was found earlier [7] that the use of the grid flow field in comparison to the serpentine one results in an approximately 30 % higher real contact pressure. These differences have to be taken into account when comparing flow field results with each other.

The fuel cell test station that operates the CCU is a commercially available test station (Evaluator C50-LT Test Station, FuelCon AG, Germany). The installed mass flow controllers strongly influence the MEA investigation according to their minimum gas flow capabilities. In our case, 0.04 L/min for anode and 0.1 L/min for cathode limits operation with a desired hydrogen stoichiometry of 1.2. Constant stoichiometry conditions will be only reached with current densities greater than ~0.2 A/cm^2, considering the active area of 20.25 cm^2 for Celtec®-P2100 MEAs.

2.1.3 Electrochemical measurements

In order to thoroughly investigate the MEA with CV, LSV, and EIS, an external potentiostat Modulab 2100A (Solartron Analytical, UK) has been connected to the test cell. For the CV and LSV measurements nitrogen was passed through the cathode (working electrode) and hydrogen through the anode (counter and pseudo-reference electrode). The CV scan started from 0.05 up to 1.0 V with a rate of 100 mV/s. LSV was performed with a potential sweep between the initial rest potential and 0.5 V with a scan rate of 2 mV/s. EIS measurements were carried out in the potentiostatic mode with the application of an alternating voltage with a perturbation amplitude of 10 mV within the frequency range from 100 kHz to 100 mHz.

2.1.4 *Compression test procedures and experimental conditions*

All MEAs under investigation followed the standard break-in procedures recommended by the respective supplier to activate the MEAs before starting normal operation. The lowest applicable pressure of 0.2 MPa has been set for this activation procedure which is necessary to achieve gas tightness. The gas supply was adjusted to constant stoichiometry $\lambda = 1.2/2.0$ with H_2 and air at a current density of 0.2 A/cm^2 ($\lambda = 1.4/2.0$ for FuMA-Tech–MEA, this stoichiometry was recommended by the supplier). Duration of the break-in procedures generally varied between 50 and 100 h. They were usually stopped once stable conditions have been reached.

The algorithm of the compression test procedure was as follows. After the break-in procedure, polarization curves and EIS measurements with H_2/air ($\lambda = 1.2/2.0$, 1.4/2.0 for FuMA-Tech–MEA) were performed. Then, the gases were switched to H_2/O_2 ($\lambda = 1.2/9.5$, 1.4/9.5 for FuMA-Tech–MEA) and polarization curves and EIS-data were recorded again. Thereafter, the gases were changed to H_2/N_2 in order to perform CV- and LSV experiments and then, to estimate the electrochemical active surface area (EASA) and hydrogen crossover, respectively. After this, the gases were reset to H_2/air ($\lambda = 1.2/2.0$, 1.4/2.0 for FuMA-Tech–MEA) and a current density of 0.2 A/cm^2 was drawn. Subsequently, the next higher contact pressure was chosen. After equilibrating overnight to reach stable conditions, the electrochemical characterization was then done for this new contact pressure.

2.2 Micro-computed tomography

The µ-CT instrument utilized in this study is the SkyScan 1172 from Bruker, Belgium. The µ-CT creates three-dimensional image volumes by merging through many separate two-dimensional radiographs taken at different angles. An extensive image processing of these two-dimensional X-ray radiographs provides three-dimensional images from the object under investigation. A detailed description of the function of a µ-CT system and the reconstruction of images including error corrections can be found here [21]. Due to simple optical geometry the resolution of a laboratory µ-CT system is much higher than clinical systems but this advantage is accompanied by the limitation that rather small sample sizes of less than 5 mm in diameter are required. Another major disadvantage of the µ-CT is that desirable investigation under real fuel cell operating conditions is currently impossible.

In case of MEAs or GDLs the sample size is determined and limited by the associated flow field which compresses the sample. To apply a defined compression on a sample in the µ-CT a suitable sample holder had to be constructed and tested for operation [22]. The adjustable contact pressure ranges between 0.5 and 2.5 MPa, dependent on the sample area size. Within a flow field land and channel areas typically alternate each other. Figure 1 shows detailed drawings of the sample holder and flow field replica. Two flow fields have been designed from polyvinylidene fluoride (PVDF) which is chemically resistive against phosphoric acid. The flow fields applied defined nominal contact pressures to the samples. With the known spring constant and flank lead rate of the main screw the nominal contact pressure could be calculated for a known sample area. It has been shown that the real contact pressure on a MEA varied largely, due to the differences between land and channel integral areas [7]. Within the flow fields the dimensions of the channel width, depth, and land width was 1 mm. From the construction and the small sample size it was obvious that a defined minimum sample size area was necessary to provide undisturbed regions of interest for investigation within the object. With this necessary sample size and the technical requirement that the actual physical dimensions of the sample holder occupied much more space in the field of view of the µ-CT instrument, the overall geometrical resolution within the images was slightly decreased.

Samples of commercially available GDL material and MEAs have been provided by external companies. Therefore, the detailed material data are proprietary and cannot be revealed within this paper.

Several samples for investigation in the µ-CT have been cut with a standard punching tool, providing sample sizes of approximately 20 mm^2. The applied contact pressures within the µ-CT compression tool are summarized in [17]. Finally, the µ-CT offers a large number of parameters to be adjusted for improvement of resolution and discriminating different kinds of errors or artifacts within the images. In order to allow reproduction of measurements, a predefined set of parameters for measurement and reconstruction had been determined with previous experiments. Table 3 provides the setting of parameters with our instrument. All images shown in the results section have been taken with this set of parameters.

3 Results and discussion

3.1 Increase of contact pressure

3.1.1 *Fuel cell testing*

In this chapter, the fuel cell performance results of three different HT-MEAs are presented. The operating temperature for all experiments was 160 °C. The aim of this chapter

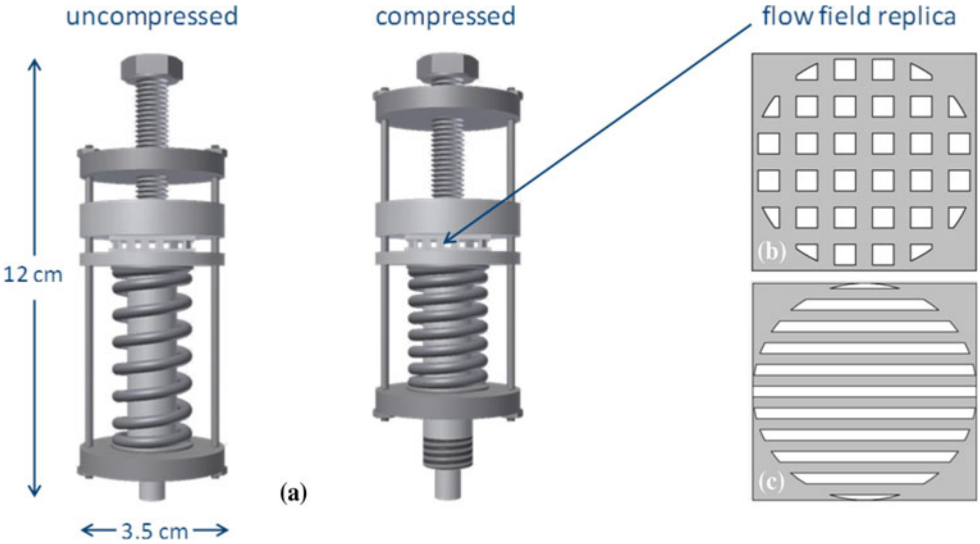

Fig. 1 Detailed *drawing* of sample holder (**a**), grid (**b**), and serpentine (**c**) flow fields replica for μ-CT

Table 3 μ-CT operational parameters for measurement

Parameters	With compression tool	Without compression tool
Acceleration voltage (kV)	78–82	78–82
Sample size	<10 mm ∅	>5 mm ∅
Rotation step (°)	0.05	0.03
Random movement	20	20
Averaging	8	8
Optical resolution (μm)	2.6	2.6
Duration (h)	Approx. 9	Approx. 16

is not to compare and, therefore, not to assess the different MEA types. A comparison is not possible in this regard insofar as the MEAs probably do not possess the same basic parameters like catalyst loadings which are required to make a reasonable comparison with respect to performance ability. Instead, the aim of this chapter is to show whether the three MEAs are influenced differently by compressive forces, and if so, to find and give explanations for that.

It shall be pointed out that the following interpretation of the MEA results has been carried out assuming that the following conceptions are valid:

- It is firstly supposed that the high-frequency resistance (HFR), the first interception with the *X* axis of a Nyquist plot at high frequencies, at high contact pressures is dominated by the proton transfer resistance of the membrane. At low contact pressures, the contact resistances at the interfaces BPP/GDL and GDL/CL are as important as membrane resistance.

HFR is the sum of the ohmic resistances of the cell components and of the electrical contact resistances. Nitta [12] has shown for a PEMFC system that (1) GDL compressive strain is logarithmically decreasing with increasing compressive stress, (2) the GDL bulk resistance was low compared to the membrane resistance, (3) the contact resistances at the interfaces BPP/GDL and GDL/CL also logarithmically decreased with increasing GDL compression, (4) the contact resistance at the interface GDL/CL was one order of magnitude larger than at BPP/GDL, and (5) the contribution of GDL/CL resistance on total resistance is comparable to the one of membrane resistance. It was pointed out by Nitta that the found high contact resistance for the GDL/CL interface was probably due to the absence of a microporous layer (MPL) coated on the used GDL. It shall further be emphasized that Nitta used a membrane with a thickness of 25 μm which was considered to be independent on compression for analysis.

The question is which of these results might be used for the analysis of the HT-MEAs in this paper. First of all, it is expected that all three MEA types contain an MPL. Thus, both contact resistances (BPP/GDL and GDL/CL) could be of similar dimension. Furthermore, membranes for HT-MEAs are much thicker than 25 μm. In Fig. 2, the experimental area-specific resistance of all three MEA types as function of contact pressure is shown, together with the calculated one for the membrane. For that calculation, two different (relatively high) conductivity values for PBI membranes and various membrane thicknesses were used. It can be seen that the experimental resistance curves illustrate a logarithmically decreasing behavior with increasing contact pressure (like it was measured by Nitta [12]) in the lower contact pressure range. In the higher contact pressure range, the curves follow more a linear trend to a varying degree depending on the MEA type (which is discussed later for the individual MEAs). In this area, the experimental curves seem to be located in the range of the calculated membrane resistance values which are a rough estimation because the exact membrane conductivity and thickness are not known by the authors.

- It is secondly assumed that proton transfer through the membrane is a linear function of membrane thickness because the specific resistance of the membrane does not change.
- It is thirdly supposed that reduction of membrane thickness is always accompanied by an increase in hydrogen crossover.

It is not assumed that a linear relationship between membrane thickness loss and hydrogen crossover rising exist because hydrogen crossover should also be heavily influenced by properties like gas permeability, membrane composition, microstructure, and environmental parameters [23]. But it is embraced that a change of these properties due to membrane thickness loss does not lead to hydrogen crossover net reduction.

3.2 BASF–MEA

Two BASF–MEAs were analyzed, one with a grid flow field and the other with a serpentine flow field. The experimental results and the resulting conclusions have been extensively discussed in a recently published paper [7]. Some of these results are shown in this paper in order to simplify the comparison with the two other MEA types. The following part not only summarizes the most important observations from [7], but it also contains extended (and partly revised) conclusions concerning the behavior of the BASF–MEAs. Figure 3 shows the MEA thickness changes as function of contact pressure and flow field geometry. Figure 4 shows the EIS of the studied MEAs at 0.3 A/cm^2 operating with H_2/air.

Both BASF–MEAs (Fig. 3a, b) show that thickness loss is logarithmically depending on contact pressure. Thickness loss is still noteworthy at the highest investigated contact pressure elevation, i.e., when increasing the contact pressure from 2.0 to 2.5 MPa, MEA thickness loss is 25 μm for the grid and 38 μm for the serpentine flow field design (Fig. 3). Even if the same real contact pressure is considered for both flow field types, MEA thickness loss is nonetheless different. The thickness changes are much smaller for the grid than for the serpentine flow field. It appears as if only the flat ending of a logarithm function can be measured for the grid flow field and the steep beginning of the curve is completely missing. This observation suggests that the MEA in the grid flow field might be pretty much compressed right from the beginning so that the following compression increase just produces only small thickness changes. It is assumed that the MEA can strongly deform itself into the channels of the grid flow field before the force sensor finally measures its initial contact pressure of 0.2 MPa. This suggestion is supported by the fact that mass transport limitation in air operation is continuously increasing with increasing contact pressure right from the beginning for the MEA in the grid flow field (Fig. 4a). The excerpt from μ-CT images showing the bulging of GDL material into the channel (Fig. 15) also supports our assumption.

Figure 5 summarizes the HFR as function of nominal contact pressure (a) and real contact pressure (b) operating with air as oxidant. Figure 6 presents the LSV curves and Fig. 7 presents the H_2 crossover collected from Fig. 6.

Contact resistance is a function of contact area and compressive force. Therefore, for the contact resistance between BPP and GDL, the land element area of the flow field is crucial. That is why the HFR chart (Fig. 5) contains both nominal and real contact pressure analysis. It can be seen that the difference in HFR between the two BASF–MEAs is smaller than 3 % for real contact pressures greater than 1.5 MPa (which corresponds to a nominal contact pressure of ∼0.57 MPa for the grid and ∼0.8 MPa for the serpentine flow field), but it is significantly higher for lower real contact pressures. Thus, flow field geometry obviously

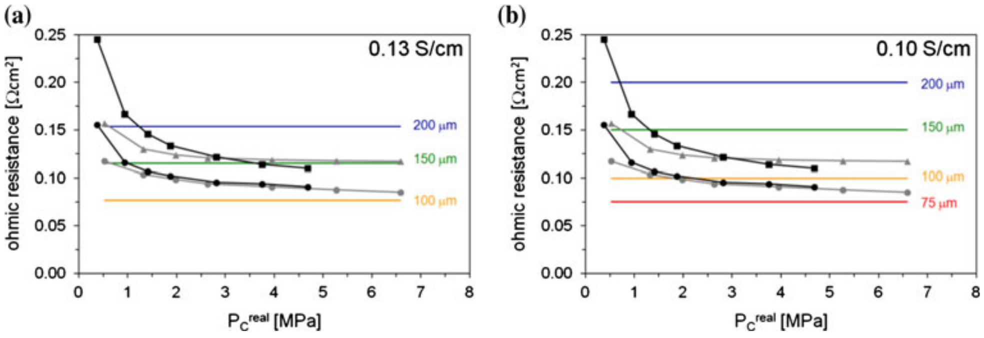

Fig. 2 Area-specific MEA resistance as function of real contact pressure for MEAs of different suppliers (*black circles*/*gray circles* BASF, *gray triangles* DPS, *black squares* FuMA-Tech) and measured with different flow field types (grid *gray*, serpentine *black*) as well as area-specific membrane resistance calculated with fixed membrane thickness and assumed membrane conductivity of 0.13 S/cm (**a**) and 0.1 S/cm (**b**)

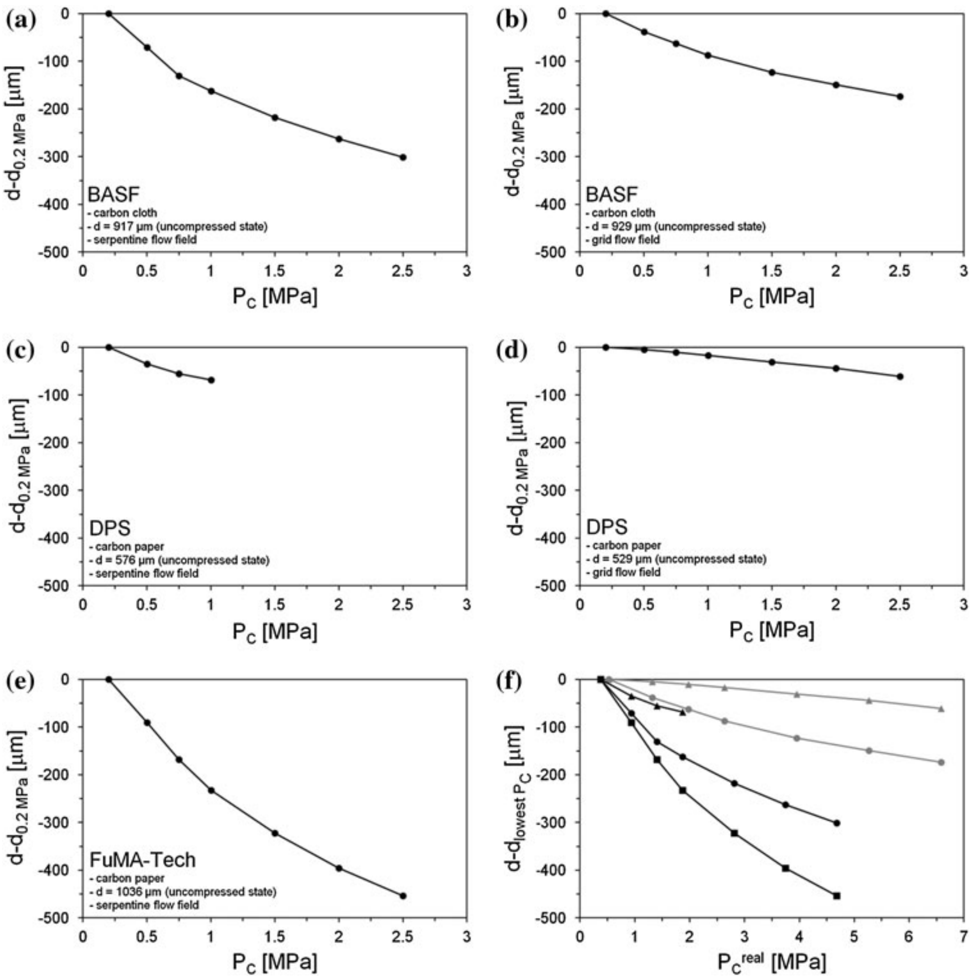

Fig. 3 MEA thickness changes as function of contact pressure for MEAs of different suppliers and measured with different flow field types. BASF–MEA (**a**, **b**), DPS–MEA (**c**), and (**d**) and FuMA-Tech–MEA (**e**). MEA thickness changes as function of real contact pressure (**f**) for *black circles*/*gray circles* BASF, *black triangles*/*gray triangles* DPS, and *black squares* FuMA-Tech (grid *gray*, serpentine *black*)

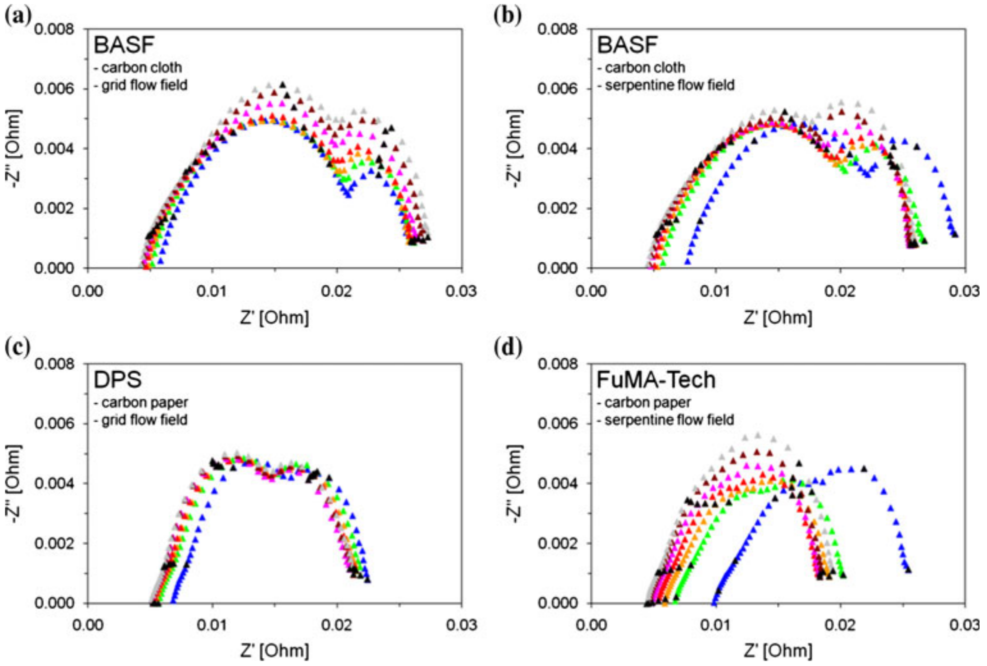

Fig. 4 Electrochemical impedance spectroscopy data at 0.3 A/cm^2 as function of contact pressure for MEAs of different suppliers and measured with different flow field types with H_2/air (BASF, DPS: $\lambda = 1.2/2.0$, FuMA-Tech: $\lambda = 1.4/2.0$), $T = 160$ °C, $p = 1$ atm (P_C in MPa: *blue* 0.2, *green* 0.5, *brown* 0.75, *red* 1, *purple* 1.5, *violet* 2, *gray* 2.5; five frequencies are each *highlighted* by *black triangles* 100 mHz, 1 Hz, 10 Hz, 100 Hz, and 1 kHz). BASF–MEA (**a**, **b**), DPS–MEA (**c**), and FuMA-Tech–MEA (**d**). (Color figure online)

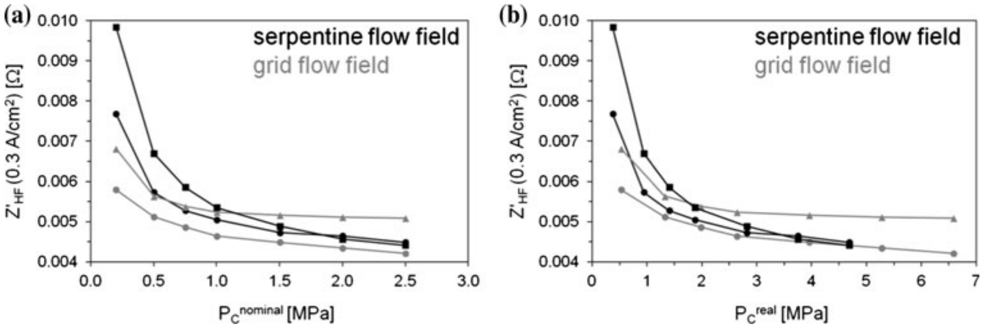

Fig. 5 High-frequency real impedance intercept as function of nominal (**a**) and real contact pressure (**b**) for MEAs of different suppliers and measured with different flow field types with H_2/air (*black circles*/*gray circles* BASF, *black triangles* DPS: $\lambda = 1.2/2.0$, *black squares* FuMA-Tech: $\lambda = 1.4/2.0$), $T = 160$ °C, $p = 1$ atm

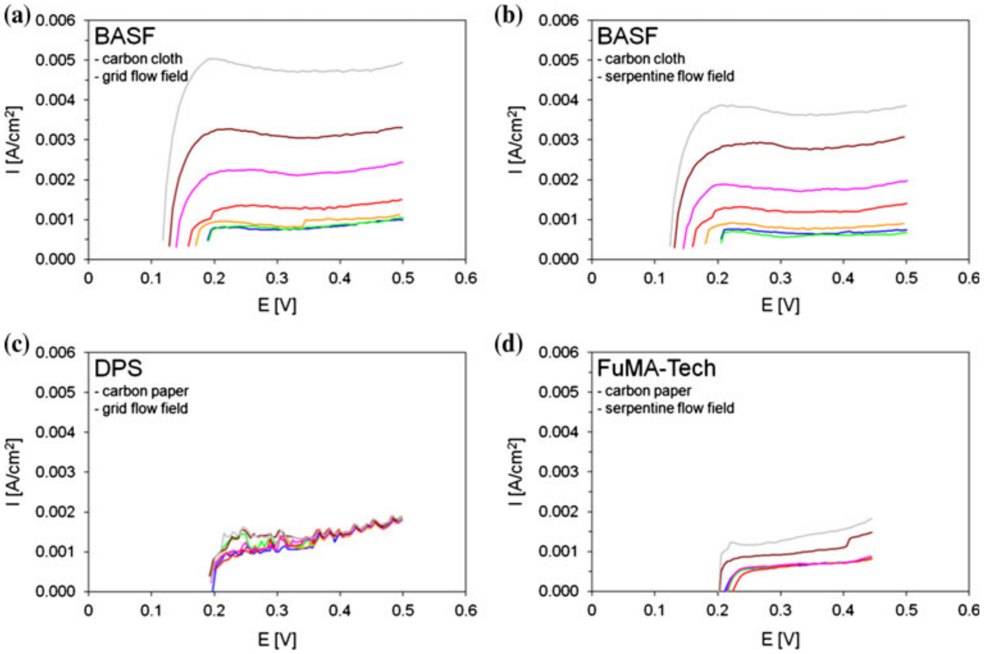

Fig. 6 Linear sweep voltammetry as function of contact pressure for MEAs of different suppliers and measured with different flow field types with H_2/N_2 (BASF 300/300 mL/min, FuMA-Tech 300/300 mL/min, DPS 100/>100 mL/min), $T = 160$ °C, $p = 1$ atm (P_C in MPa: *blue* 0.2, *green* 0.5, *brown* 0.75, *red* 1, *purple* 1.5, *violet* 2, *gray* 2.5; curves for BASF with electrical short correction for $P_C \geq 0.75$ MPa). BASF–MEA (**a**, **b**), DPS–MEA (**c**), and FuMA-Tech–MEA (**d**) (*left* grid flow field, *right* serpentine flow field). (Color figure online)

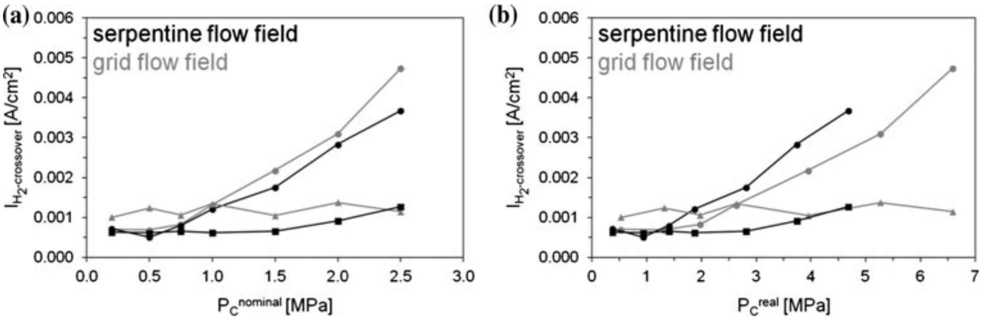

Fig. 7 Limiting hydrogen crossover current as function of nominal (**a**) and real contact pressure (**b**) for MEAs of different suppliers and measured with different flow field types with H_2/N_2 (*black circles*/*gray circles* BASF, *black squares* FuMA-Tech 300/300 mL/min, *black triangles* DPS 100/>100 mL/min), $T = 160$ °C, $p = 1$ atm; values for BASF with electrical short correction for $P_C \geq 0.75$ MPa

has an effect on HFR for real contact pressures below 1.5 MPa. The thickness analysis has previously revealed that the MEA in the grid flow field must be more compressed than the one in the serpentine flow field because the different flow field geometry causes a different deformation behavior of the MEA into the flow field channels. As no change in hydrogen crossover can be observed for both MEAs in this contact pressure range (Figs. 6, 7, please see also discussion further below in this chapter), no change in membrane thickness and, therefore, no change in proton transfer resistance could have occurred. That means the gap in HFR at lower real contact pressures between the two flow field types must have its origin in a different contact resistance. Two possible kinds of contact resistance could play a role. Either the contact resistance at the interface BPP/GDL or the contact resistance at the interface GDL/CL is concerned or both of these contact resistances are influenced. The quadratic blocks of the grid flow field can entrench themselves better into the flexible GDL material of the BASF–MEA than the ribs of the serpentine flow field (please refer to [7] for flow field schemes) and, therefore, more GDL surface is in contact with the graphite collector which reduces the BPP/GDL contact resistance for the MEA in the grid flow field. A lower contact resistance at the interface GDL/CL could be explained by a better serration of GDL and CL through compression which results in a larger contact area between these two layers and, therefore, in less contact resistance at this interface; as the MEA in the grid flow field is more compressed, it possesses the lower HFR. From these experiments it cannot be concluded which of the contact resistances is influenced by compression and to what degree. But contact pressure cycling experiments gives very interesting results into the interface contact resistances (see section below). Above a real contact pressure of about 2.5 MPa, the HFR of both MEAs almost linearly decreases with increasing compression. That means membrane thickness loss takes place here. The HFR decreases about 5 % when the real contact pressure is increased from 2.5 to 4.5 MPa. Proportionality between resistance and distance would mean that membrane thickness loss accounts for 5–10 µm in this contact pressure range. BASF–MEA component dimensions (two GDL with each 350–400 µm, one membrane with 100–200 µm) have already hinted that an observed MEA thickness loss of up to 300 µm (Fig. 3f) must be mainly caused by GDL compression, but that membrane compression obviously plays such a minor role in MEA thickness loss is nonetheless surprising.

CVs as function of contact pressure are presented in Fig. 8. The area under the H_2 desorption peak curve region (from ~0.05 to ~0.34 V) is directly correlated to EASA as it was commented in the experimental section. Therefore, in this manuscript, when the authors write about an EASA it is also in relation to the H_2 desorption peak observed in a CV.

The EASA has actually not changed with increasing compressive pressure (Fig. 8). As the phosphoric acid content in the membrane is about 95 wt% and marginal membrane thickness loss takes place at higher contact pressures, at least some acid should be squeezed out of the membrane. As the EASA has not changed, it must be concluded that all catalyst sites have been in contact with phosphoric acid already at the lower contact pressures. Thus, the idea that EASA could be used as tool to prove that phosphoric acid is squeezed out of the membrane at high contact pressures, at least not for this MEA type, has not worked.

For both BASF–MEAs, hydrogen crossover seems to be pretty similar for lower nominal contact pressures up to 0.75 MPa, but it is drastically increasing for higher contact

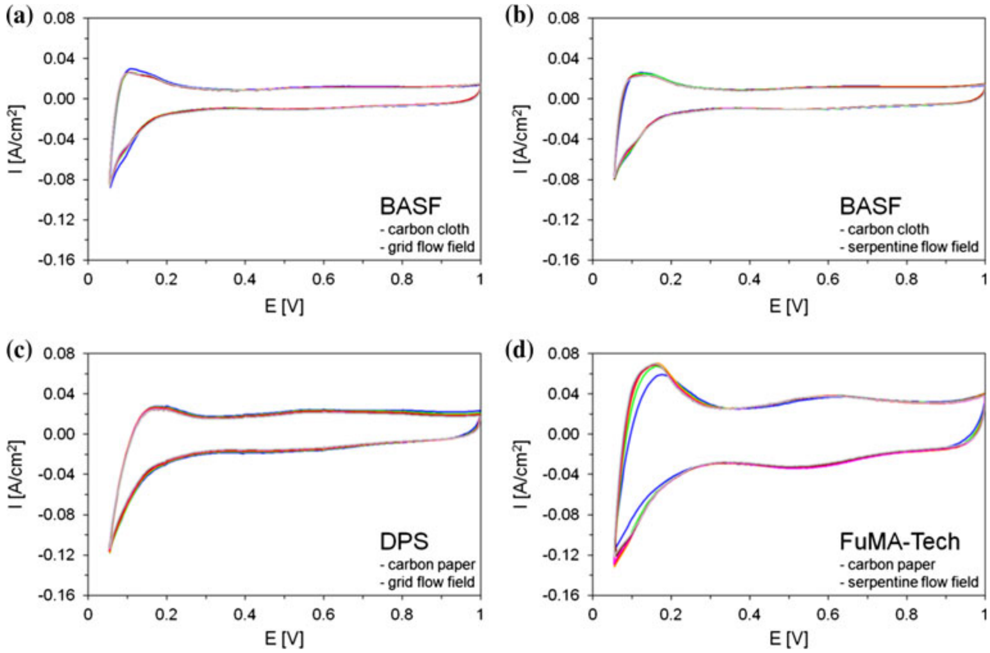

Fig. 8 Cyclic voltammetry as function of contact pressure for MEAs of different suppliers and measured with different flow field types with H_2/N_2 (BASF, FuMA-Tech 100/100 mL/min, DPS 100/>100 mL/min), $T = 160$ °C, $p = 1$ atm (P_C in MPa: *blue* 0.2, *green* 0.5, *brown* 0.75, *red* 1, *purple* 1.5, *violet* 2, *gray* 2.5; *curves* for BASF with electrical short correction for $P_C \geq 0.75$ MPa). BASF–MEA (**a**, **b**), DPS–MEA (**c**), and FuMA-Tech–MEA (**d**) (*left* grid flow field, *right* serpentine flow field). (Color figure online)

pressures (Fig. 7). The LSV experiment with the MEA in the serpentine flow field shows (Fig. 7b) that the absolute value for low hydrogen crossover currents must be cautiously regarded. It can be seen that a lower hydrogen crossover current was measured at 0.5 MPa than at 0.2 MPa. Obviously, the experimental set-up used for hydrogen crossover determination is not as precise as desired and only qualitative analysis is possible, at least for low hydrogen crossover currents. No obvious change in hydrogen crossover means that no change in membrane thickness could have taken place when the nominal contact pressure was increased up to 0.75 MPa. According to Fick's law [24], diffusion is inversely proportional to pathway length. The proton transfer resistance indicates a change of 5 % for the membrane thickness when changing the real contact pressure from 2.5 to 4.5 MPa, but the observed increase in hydrogen crossover is much higher. It was illustrated in [7] that strong electrical short circuit formation is simultaneously taking place when hydrogen crossover rises. Therefore, all signs indicate that the source which triggered the loss in electrical short resistance is also responsible for that hydrogen crossover increase. The reason could be penetration of GDL fibers (Fig. 17b, e) into the membrane by too high compressive pressure and thus creation of a pinhole which enormously facilitates gas species crossover so that the theory of pure hydrogen diffusion is not valid in this case.

Figure 9 shows polarization curves and Fig. 10 presents selected points of polarization curves as function of contact pressure operating with H_2/air. As it can be seen in Figs. 9 and 10, both hydrogen crossover and electrical shorting lower the cell voltage and are more noticeable when less current is drawn from the cell. That is why the polarization curves exhibit the strong voltage drop at open circuit voltage and lower current densities with increasing contact pressure. Moreover, the polarization resistance of the cell impedance recorded at a certain potential is equal to the negative slope of the polarization curve at the same potential. That means, the gentler the slope of the polarization curve is, the smaller the impedance spectrum gets. Nyquist plots of the MEAs operating with H_2/O_2 must be included (Fig. 11) because it may not be well seen in the IV-curves that the slope of the polarization curve at a current density of 0.3 A/cm^2 is still affected by electrical shorting, but the impedance spectra in oxygen operation mode (Fig. 11a, b) clearly show that the size of the impedance spectrum decreases at the same moment when electrical short formation starts.

Measurements with pure oxygen at cathode side are always interesting insofar that the results are not influenced by mass transport limitation effects. Thus, Fig. 12 presents the polarization curves and Fig. 13 shows the selected points of polarization curves as function of contact pressure operating with H_2/O_2. As it can be seen from Fig. 12a, the iR-corrected IV-curve at 0.2 MPa for the MEA in the grid flow field is slightly higher than the curves at higher contact pressures. This also holds true to a lesser extent for the MEA in the serpentine flow field. The CV (Fig. 8) reveals that the hydrogen desorption peak (and, therefore, EASA) is slightly bigger at this contact pressure. The reason for this observation probably is that the whole experiment had started at the lowest contact pressure of 0.2 MPa and, therefore, the initial catalyst stabilization—which leads to

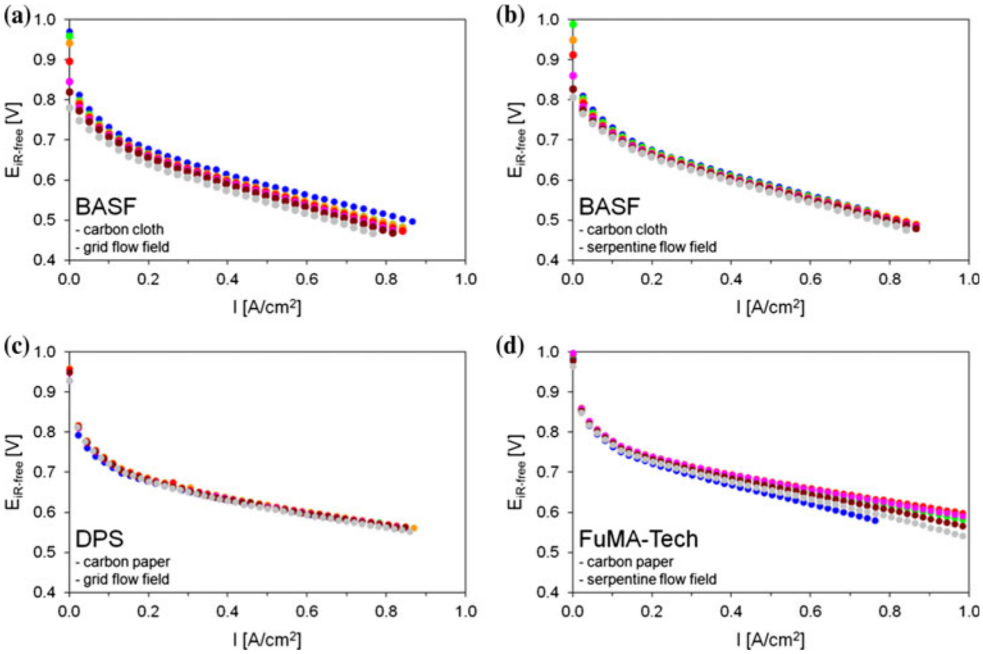

Fig. 9 iR-corrected polarization *curves* as function of contact pressure for MEAs of different suppliers and measured with different flow field types with H_2/air (BASF, DPS: $\lambda = 1.2/2.0$, FuMA-Tech: $\lambda = 1.4/2.0$), $T = 160$ °C, $p = 1$ atm (P_C in MPa: *blue* 0.2, *green* 0.5, *brown* 0.75, *red* 1, *purple* 1.5, *violet* 2, *gray* 2.5). BASF–MEA (**a**, **b**), DPS–MEA (**c**), and FuMA-Tech–MEA (**d**) (*left* grid flow field, *right* serpentine flow field). (Color figure online)

Fig. 10 Selected *points* of iR-corrected polarization *curves* as function of contact pressure for MEAs of different suppliers and measured with different flow field types with H_2/air (BASF, DPS: $\lambda = 1.2/2.0$, FuMA-Tech: $\lambda = 1.4/2.0$), $T = 160$ °C, $p = 1$ atm (j in A/cm^2: *black* 0, *dark blue* 0.1, *green* 0.2, *yellow* 0.3, *orange* 0.4, *red* 0.5, *purple* 0.6, *brown* 0.7, *gray* 0.8, *light blue* 0.9, *violet* 1.0). BASF–MEA (**a**, **b**), DPS–MEA (**c**), and FuMA-Tech–MEA (**d**) (*left* grid flow field, *right* serpentine flow field). (Color figure online)

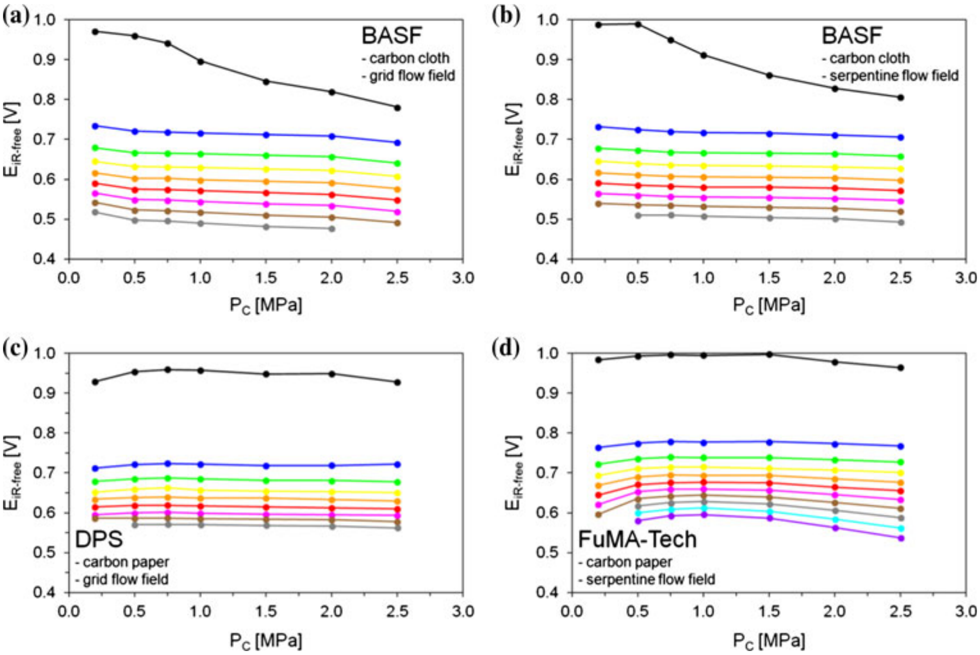

Fig. 11 Electrochemical impedance spectroscopy data at 0.3 A/cm^2 as function of contact pressure for MEAs of different suppliers and measured with different flow field types with H_2/O_2 (BASF, DPS: $\lambda = 1.2/9.5$, FuMA-Tech: $\lambda = 1.4/9.5$), $T = 160$ °C, $p = 1$ atm (P_C in MPa: *blue* 0.2, *green* 0.5, *orange* 0.75, *red* 1, *purple* 1.5, *brown* 2, *gray* 2.5; five frequencies are each *highlighted* by *black triangles* 100 mHz, 1 Hz, 10 Hz, 100 Hz, and 1 kHz). BASF–MEA (**a**, **b**), DPS–MEA (**c**), and FuMA-Tech–MEA (**d**) (*left* grid flow field, *right* serpentine flow field). (Color figure online)

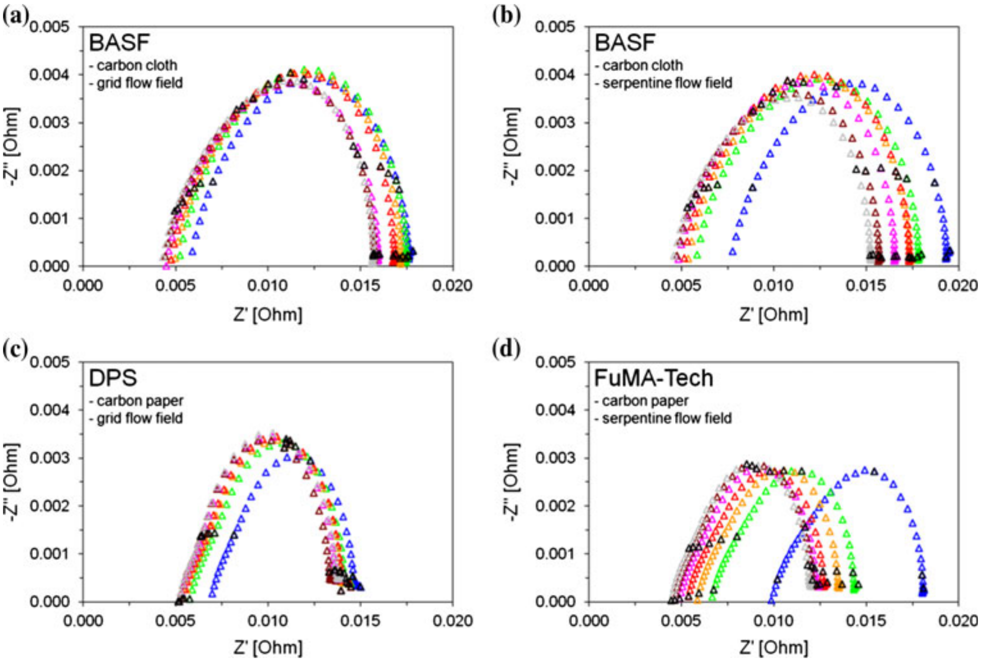

initial EASA loss—has not finished yet when the characterization at this first contact pressure was carried out.

3.3 FuMA-Tech–MEA

The FuMA-Tech–MEA was measured with the serpentine flow field. As the flow field analysis with BASF–MEAs has shown a high impact of flow field geometry on fuel cell performance, it makes sense to compare the FuMA-Tech–MEA with the BASF–MEA which was also measured with the serpentine flow field.

The FuMA-Tech–MEA is 10 % thicker than the BASF–MEA, but its thickness loss is 20 % higher. At a contact pressure of 2.5 MPa, the MEA is reduced to nearly 50 % of its initial thickness (Fig. 3e). That means the FuMA-Tech–MEA can be compressed more than the BASF–MEA. The question again is what parts of MEA thickness loss result from GDL and membrane compression, respectively. Combined analysis of HFR (Fig. 5) and hydrogen crossover (Fig. 7) shows that up to a nominal contact pressure of 1.5 MPa, the HFR strongly decreases while no change in hydrogen crossover can be observed. That means only

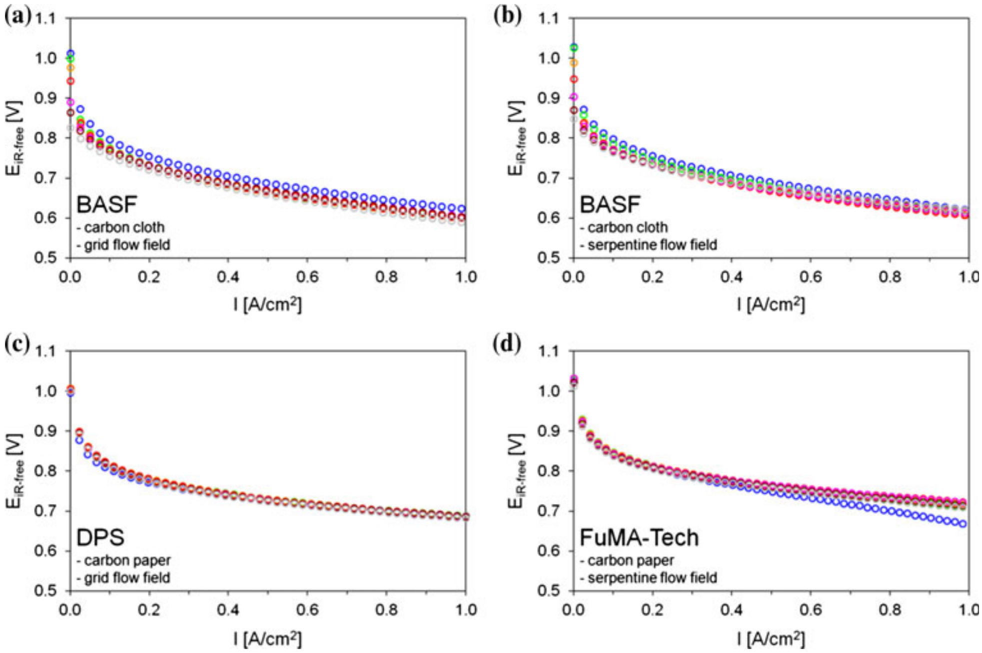

Fig. 12 iR-corrected polarization *curves* as function of contact pressure for MEAs of different suppliers and measured with different flow field types with H_2/O_2 (BASF, DPS: $\lambda = 1.2/9.5$, FuMA-Tech: $\lambda = 1.4/9.5$), $T = 160$ °C, $p = 1$ atm (P_C in MPa: *blue* 0.2, *green* 0.5, *orange* 0.75, *red* 1, *purple* 1.5, *brown* 2, *gray* 2.5). BASF–MEA (**a**, **b**), DPS–MEA (**c**), and FuMA-Tech–MEA (**d**) (*left* grid flow field, *right* serpentine flow field). (Color figure online)

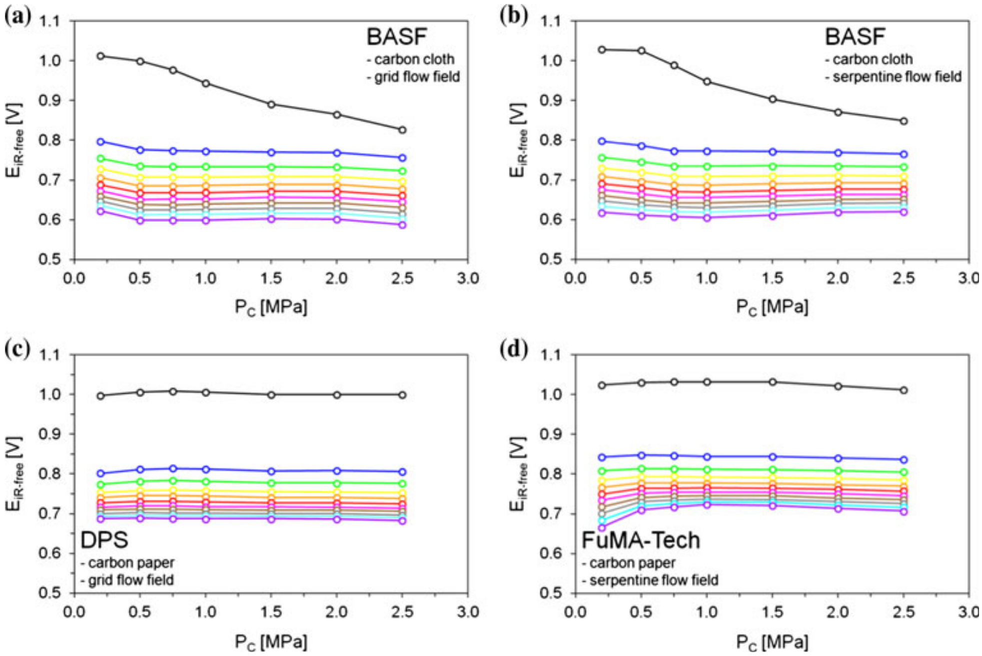

Fig. 13 Selected *points* of iR-corrected polarization *curves* as function of contact pressure for MEAs of different suppliers and measured with different flow field types with H_2/O_2 (BASF, DPS: $\lambda = 1.2/9.5$, FuMA-Tech: $\lambda = 1.4/9.5$), $T = 160$ °C, $p = 1$ atm (j in A/cm^2: *black* 0, *dark blue* 0.1, *green* 0.2, *yellow* 0.3, *orange* 0.4, *red* 0.5, *purple* 0.6, *brown* 0.7, *gray* 0.8, *light blue* 0.9, *violet* 1.0). BASF–MEA (**a**, **b**), DPS–MEA (**c**), and FuMA-Tech–MEA (**d**) (*left* grid flow field, *right* serpentine flow field). (Color figure online)

GDL compression is taking place up to that point. From 1.5 to 2.5 MPa, the HFR is decreasing about 10 % while hydrogen crossover current is nearly doubling. In contrast to BASF, no significant electrical short circuit formation takes place in the analyzed contact pressure range (Fig. 6c). Therefore, the observed hydrogen crossover current must be solely attributed to a thinner membrane. Thus, the amount of hydrogen diffusion is higher than it was expected from the anticipated membrane thickness loss (which must be even lower than 10 % because the HFR value at 1.5 MPa is still slightly affected by the logarithmic part of the curve). So, this analysis had shown that the relationship between membrane thickness and hydrogen crossover change is more complicated. There are two alternatives. One explanation could be that proportionality between proton transfer resistance and distance (i.e., membrane thickness) can probably be assumed, but further parameters (except distance) which are relevant for hydrogen crossover have changed. The second explanation could be that the relative error in hydrogen crossover measurement is high, especially for low current values (see also Sect. 3.2 of BASF–MEA), so that a quantitative relationship between HFR and hydrogen crossover cannot be achieved.

But an increase in hydrogen crossover at 2 and 2.5 MPa must have taken place because OCV loss appears at these contact pressures (Figs. 10d, 12d), even in oxygen-operating mode. It can further be seen that OCV is also smaller at the lowest contact pressure of 0.2 MPa. The iR-corrected IV-curve for oxygen operation mode (Fig. 12d) shows that not only the OCV but also the total performance is not good at this contact pressure. A much smaller EASA at 0.2 MPa is the reason as the CV precisely illustrates (Fig. 8). This is in contradiction to the results for the BASF–MEAs. Varying manufacturing procedures may be responsible for this difference. It is imaginable that in the FuMA-Tech–MEA only the membrane is doped with phosphoric acid but not the GDE. Therefore, a complete three-phase reaction zone is not obtained before a certain compression has been reached which provides the release of some kind of excess phosphoric acid out of the membrane into the GDE. The big hydrogen desorption peak of the FuMA-Tech–MEA suggests that more catalyst is used here than for BASF–MEAs. If it is assumed that both MEA suppliers use firstly a similar Pt/C metal loading to achieve high catalyst surface and secondly carbon supports with similar surfaces, then a higher platinum amount results in a thicker CL. This could explain why for the FuMA-Tech–MEA a certain compression level is needed to bring all catalyst sites in contact with the phosphoric acid. The amount of the apparently used excess phosphoric acid must be nonetheless minor because no effect in hydrogen crossover (and, therefore, in membrane thickness) can be observed.

The optimum nominal contact pressure for FuMA-Tech–MEA is about 1 MPa as the iR-corrected polarization curve in air-operating mode shows (Fig. 9d). Impedance analysis reveals that mass transport limitation gets stronger at higher contact pressures (Fig. 4d).

In summary, FuMA-Tech–MEA analysis has also shown that the percentage of membrane compression on the total MEA thickness loss is low. The HFR chart (Fig. 5) shows that no difference in HFR between the FuMA-Tech–MEA and BASF–MEA exists at high contact pressures. If one assumes that the different used polymer backbones do not impact the proton transfer ability of the membrane, then it must be concluded that the membrane thicknesses of the two MEA types are in the same range; as the membrane compression does not significantly contribute to the overall MEA thickness loss for both MEA types, it must be concluded that both suppliers use membranes with similar thicknesses. Therefore, the higher initial thickness of the FuMA-Tech–MEA must come from a thicker GDL. With regard to percentage, the thickness loss by compression is higher than it should be compared to the original thickness gain by a thicker GDL. Thus, the GDL material of the FuMA-Tech–MEA must be more compressible than the one of the BASF–MEA. FuMA-Tech uses carbon paper as GDL material, while BASF uses carbon cloth. Here, the non-woven structure is obviously not only thicker but also softer than the woven material.

3.4 DPS–MEA

The DPS–MEA was measured with the grid flow field. Therefore, the DPS–MEA will be compared with the BASF–MEA which was also measured with the grid flow field.

The DPS–MEA thickness is 539 μm which is much thinner in the uncompressed state than the two other MEA types (Fig. 3). Therefore, it is no wonder that the overall MEA thickness loss with increasing contact pressure is much less when compared to the other two MEA types. But even when the initial thickness is taken into account, the percentage thickness loss is lower. It was shown in literature [25] that carbon paper is less compressible than carbon cloth. It can further be seen that the thickness loss curve does not show this logarithmic dependency from contact pressure as it was shown by the other MEAs. The authors think that the combination of MEA stiffness (see below) and the arrangement of the land elements in the grid flow field might be responsible for that. Another DPS–MEA which was from another batch seems to show the actually anticipated logarithmic curve shape. But these data were from an experiment for which the serpentine flow field was used (Fig. 3c). Besides, that experiment does not cover the desired contact pressure range (and is, therefore, not considered in this paper).

Apart from the MEA thickness loss curve (Fig. 3d) as well as the behavior at a contact pressure of 0.2 MPa (Fig. 9c), it can be stated that the DPS–MEA is practically immune against contact pressure variation. Fuel cell performance, HFR, EASA, hydrogen crossover, and mass transport limitation show no noteworthy change. The LSV experiment with the DPS–MEA shows that the current fluctuation was quite high (Fig. 6c). The reason was that the applied hydrogen flow was lower than for the measurements of the other MEA types. It can be further noticed that the hydrogen desorption peak in the CV chart (Fig. 8c) is very small. The main reason is that a too high nitrogen flow rate was unfortunately applied during the CV measurements for this MEA; the nitrogen flow rate has an immense impact on size and shape of the hydrogen desorption peak as Schneider et al. [26] had pointed out.

For a contact pressure of 0.2 MPa, the HFR is much higher than that for the other contact pressures (Fig. 5). The following contact pressure increase to 0.5 MPa significantly reduces the HFR while MEA thickness loss is insignificant. No contact pressure cycling experiment was carried out with this MEA type so that no final statement can be made whether the electrical contact at the BPP/GDL or at the GDL/CL interface is responsible for that. Considering the results from the contact pressure cycling experiments with the BASF–MEAs, it is assumed that the first one is the reason. When mounting the MEA, it was already noticed that this MEA type is quite stiff compared to FuMA-Tech–MEA and BASF–MEA so that compression, not to mention deformation into the flow field channels, does not seem to happen for the DPS–MEA; at least not before a nominal contact pressure of 0.75 MPa is reached as the MEA thickness loss curve indicates (Fig. 3d). But although the thickness curve does not show a noticeable loss before 0.75 MPa, the electrical contact between BPP and GDL must have improved because a decrease in HFR can be observed. Therefore, it is absolutely imaginable that the graphite collector barely touches the MEA at 0.2 MPa. Another noteworthy observation at 0.2 MPa is that the slope of the IV-curve measured with oxygen (Fig. 12c) is less steep at low current densities which reduces the size of the impedance spectrum (Fig. 11c). A very close look on the CV (Fig. 8c) shows that the curve is a little bit tilted at 0.2 MPa as if it is overlaid by a small linearly increasing current. For BASF–MEAs, this happened at high contact pressures and was explained with the formation of an electrical short circuit through GDL fiber penetration into the membrane. For the DPS–MEA, there must be a connection between the bad current conduction at the BPP/GDL interface and this observable minor electrical short circuit. Maybe the apparently high contact resistance between GDL and BPP hampers the electron dissipation from the GDL; as the membrane is not a perfect isolator, a short circuit current is generated. A further observation at 0.2 MPa is that the OCV must be influenced by a mass transport effect. It can clearly be seen that the difference to the OCV at the next higher contact pressure of 0.5 MPa is much bigger in air-operating mode (Fig. 10c) than in oxygen-operating mode (Fig. 13c). In air-operating mode the OCV at 0.5 MPa seems also to be influenced by that effect. It was mentioned above that the MEA is not deformed at all below 0.75 MPa. Therefore, the longer diffusion path length from the channels to the catalyst sites obviously becomes noticeable.

A significant difference to both BASF–MEA and FuMA-Tech–MEA is that the HFR (Fig. 5) is a constant value at higher contact pressures for the DPS–MEA. That means that this membrane is obviously completely incompressible in the analyzed contact pressure range. Therefore, the MEA thickness loss for the DPS–MEA must solely come from GDL compression which is not accompanied by detectable mass transport limitation although the OCV value in air-operating mode (Fig. 10c) indicates that a mass transport effect must nonetheless occur at the highest contact pressure of 2.5 MPa. It shall further be noted that the membrane resistance is higher for the DPS–MEA than for the other two MEA types. This can be explained by the lower phosphoric acid amount which is used for the membrane in the DPS–MEA.

The main result from the fuel cell testing with HT-MEAs of three different suppliers is that the applied compressive pressure obviously has a main impact on GDL compression, but the effect on membrane compression is surprisingly small. Therefore, membrane thinning by compression is obviously not as strong as generally assumed.

3.4.1 Micro-computed tomography

The μ-CT technique was applied to see whether the suggestions about the structural behavior of the MEA in the flow field concluded from fuel cell testing can finally be confirmed. This has been done exemplarily with BASF–MEAs only which have been investigated for this paper with the grid flow field design.

Figure 14 shows a sample of a fresh and uncompressed MEA in the μ-CT as a reference to the following images. The structure of the MEA can easily be identified on the GDL fibers, CLs, and the membrane in the center.

Figure 15 now shows detailed images of a MEA under compression, the blue-framed images refer to 0.2 MPa, the gray to 2.5 MPa as compression force. The bulging of the GDL material into the channel under high compression can easily identified on the upper right. The resolution within these images is slightly poorer than the uncompressed one, due to usage of the required compression tool (whose impact on image quality was previously described).

For Fig. 16, MEA thickness values under the land and inside the channel of the flow field were determined at four

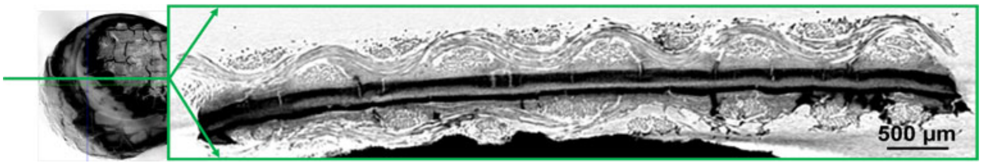

Fig. 14 μ-CT *image* of an original uncompressed MEA sample as reference. The *green line* represents the slicing position of the *image* within the three-dimensional sample. (Color figure online)

Fig. 15 μ-CT *images* for comparison of a MEA in the compression tool (channel and land area of the flow field) showing the effect of bulging into the channel area as well as the breaking of the catalytic layer (*red circle*). *Colored frames* for compression forces: *blue* 0.2 MPa, *gray* 2.5 MPa. (Color figure online)

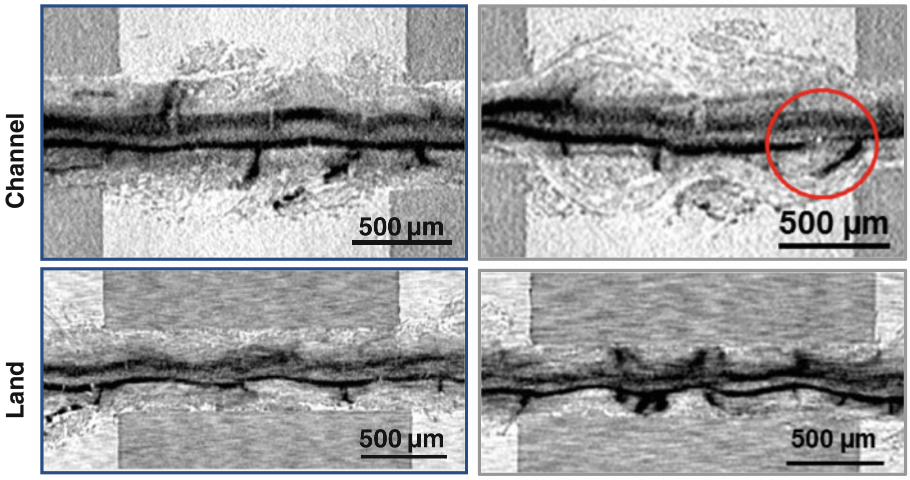

different contact pressures. It can be seen that the bulging into the channel roughly follows an increasing logarithmic function with increasing contact pressure. This bulging is strongly taking place at the beginning of contact pressure rising and slows down the higher the contact pressure gets. Thus, the assumption from MEA thickness loss analysis in the fuel cell testing section is confirmed that due to the good GDL deformation ability the MEA must be much compressed before the desired contact pressure is achieved, at least for the lower contact pressures. It can further be observed that MEA thickness under the land element is logarithmically decreasing with increasing contact pressure. The thickness determination for both under the land and inside the channel was not easy. That is why ten random spots were used to determine an average thickness value. Inside the channel, the thickness determination is complicated by the rather low contrast between GDL material and air in the channel. Another reason is that the bulging does not always happen symmetrically. This might be due to the MEA manufacturing process and the utilized materials. Variation in thickness determination under the land element could be explained with the woven structure of the GDL. It is imaginable that the deformation behavior could depend on where exactly the flow field land element presses on the woven structure, e.g., whether it is directly on a knot or a little bit next to it. But in spite of the errors in determining absolute thickness values, the different trends for the MEA thickness as function of contact pressure are clearly visible for the two flow field regions.

What cannot be clearly identified is the possibility of shear forces moving the anode or cathode layers slightly differently against each other into the channel. This could lead to delaminating between the layers which might be possible to be visualized within μ-CT images. So, further investigation is required to better understand the mechanical behavior of a MEA under compression and under various flow field designs.

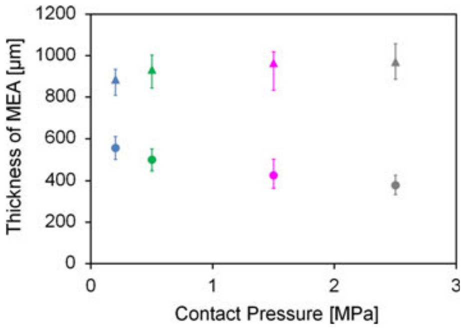

Fig. 16 MEA thicknesses within a channel and under land of a grid flow field, analyzed with μ-CT and averaged over ten randomly values for each data point (*black triangles* channel, *black circles* land)

Figure 17 shows a μ-CT two-dimensional image sliced at a defined position (green line) through a compressed MEA which was removed from the compression tool before investigation. Since three-dimensional imaging, especially in μ-CT with two-dimensional slices from different point of views, is sometimes difficult to understand we present a short explanation. Figure 17a provides an overview on the whole sample from the top, but already inside the layer structure so that the two-dimensional image (b) is physically located right above the CL. The cathode lies above, the anode below the membrane which is the light gray line in the center. The green line marks the actual view through the sample given in (b). Figure 17c–e are enlarged excerpts showing different effects. In (c), within the large red circle, we see fibers from the GDL penetrating into the CL. The white "line" within the small red circle could be a CL defect caused by compressive stress but it is also possible that it is a drying crack coming from the CL production procedure. In Fig. 17d, e, GDL fiber penetration through the CL into the membrane is shown. Therefore, the observed electrical short circuit formation during the fuel cell testing experiments with BASF–MEAs can really be attributed to that cause.

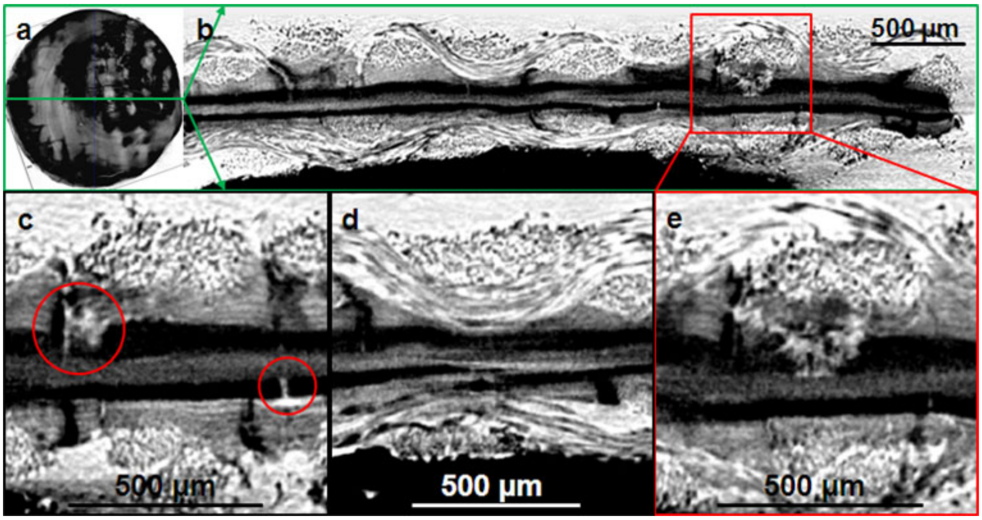

Fig. 17 µ-CT *image* (**b**) after 2.5 MPa compression (removed from the compression tool) at a defined position (**a**), including also three enlarged excerpts (**c–e** to identify physical damages through high compression forces)

GDL fiber piercing through the MPL can also be seen on the SEM image (Fig. 18) which has been taken after 22 h of compression at 2.5 MPa and 2 weeks of relaxation time after removal from the compression tool, leaving only irreversible damage effects to be imaged.

In summary, the µ-CT measurements confirm the assumption from the electrochemical experiments that the MEA deforms itself into the flow field channels. The bulges could clearly be seen. It was also seen that the MEA thickness under the flow field land elements decreases with increasing contact pressure. It is furthermore confirmed that GDL fiber penetration into the membrane is the source for the measured electrical short formation and hydrogen crossover increase, respectively.

What has not been thoroughly investigated yet is the more detailed effect of compression on the pore structures of the different layers, for example porosity changes by mechanical deformation and/or crushing of pores. So a direct relation to mass transport effects cannot be clearly shown at this point of time. Further improvement on the compression tool (no metallic components) and improved image processing methods should enhance our understanding of the effects of compression on a MEA in the near future.

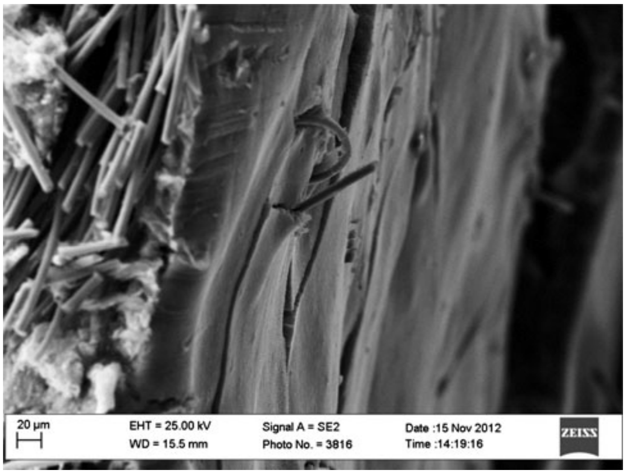

Fig. 18 SEM *image* showing *broken* GDL *fibers* that have pierced the catalytic layer

3.5 Contact pressure cycling

An interesting question is if the compression and the resulting effects on fuel cell properties are reversible. Therefore, contact pressure cycling experiments were carried out with BASF–MEAs for both the serpentine (Fig. 19) and grid flow field (Fig. 20).

Both MEAs show that the MEA thickness change consists of both a reversible and irreversible part. If the MEA is compressed to the highest contact pressure (here 1.5 MPa) for the first time, the following compressive force reduction does indeed lead to an increase of the MEA thickness again. But this thickness gain is smaller than the previous total thickness loss. When the second contact pressure cycle is fulfilled and the compressive force reduction is carried out again, then the MEA thickness recovers to almost the same starting value of the second cycle, at least for the MEA in the grid flow field. For the MEA in the serpentine flow field, it takes one cycle longer. The reason is that this MEA is not as much compressed right from the beginning as the MEA in the grid flow field. It was shown by compressive force cycling tests [25] that GDL elasticity loss occurs which is especially strong in the first compression and that this residual strain apparently approaches a constant value over time.

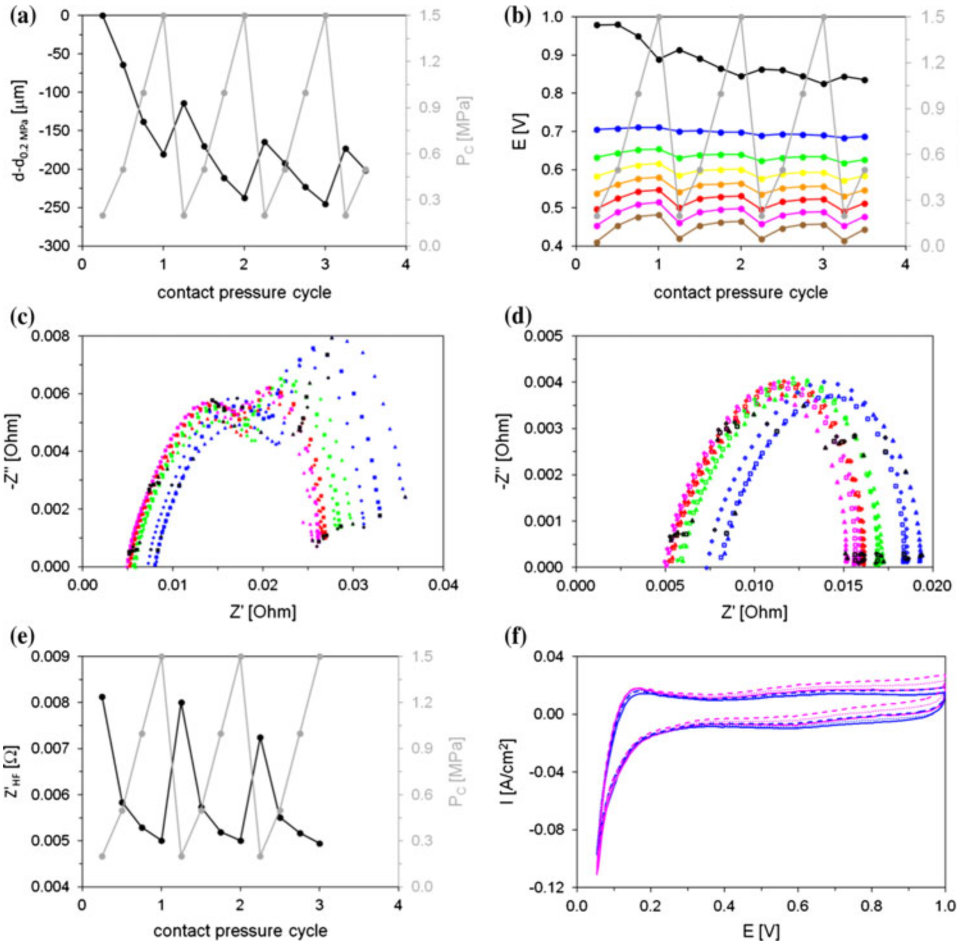

Fig. 19 MEA thickness changes (**a**), selected *points* of IV-curve (**b**), EIS-spectrum at 0.3 A/cm^2 with air (**c**) and oxygen (**d**), high-frequency resistance at 0.3 A/cm^2 (**e**), and cyclic voltammetry (**f**) as function of contact pressure cycling of BASF–MEA at 160 °C, 1 atm, *serpentine flow field* with H_2/air ($\lambda = 1.2/2$) [**b**, **c**, **e**], H_2/O_2 ($\lambda = 1.2/9.5$) [**d**], and with H_2/N_2 [**f** 0.1/>0.1 L/min] (**b** j in A/cm^2: *black* 0, *dark blue* 0.1, *green* 0.2, *yellow* 0.3, *orange* 0.4, *red* 0.5, *purple* 0.6, *brown* 0.7, **c**, **d**, **f** P_C in MPa: *blue* 0.2, *green* 0.5, *red* 1, *purple* 1.5, **c**, **d** contact pressure cycle: *black triangles* first, *black squares* second, *black diamonds* third, **f** contact pressure cycle: *continuous lines* first, *dotted lines* second, *dashed lines* third). (Color figure online)

Both MEAs further illustrate that the OCV values from 0.2 to 1 MPa of the first cycle are not reached again in the following cycles. It can be seen that the OCV recovers a little bit each time the contact pressure reduction from 1.5 to 0.2 MPa takes place. But if one compares the OCVs at a certain contact pressure of each cycle (e.g., all OCV values at 1 MPa), an on-going decline can be observed for the OCV. The reason is that electrical short circuit formation was again triggered at the highest chosen contact pressure of 1.5 MPa. Therefore, the previously reported short circuit formation was no coincidence. The BASF–MEAs seems to be prone to that phenomenon. Unfortunately, no LSV experiments were conducted for the contact pressure cycling experiments. Moreover, the CV experiments were carried out with a too high nitrogen flow rate on the cathode side so that the hydrogen desorption peaks are small again, but the tilting in the CVs because of short circuit current can definitely be used for interpretation. For better clarity only the CVs at 0.2 and 1.5 MPa are presented. The electrical short circuit is again not as bad for the MEA in the serpentine flow field as for the one in the grid flow field, because the MEA in the serpentine flow field is not as much compressed as the one in the grid flow field. It can be seen that the CVs at 0.2 MPa of the first and second cycle possess the same tilting for the MEA in the serpentine flow field. The CV at 0.2 MPa of the third cycle exhibits a stronger tilting. The reason for that is that the MEA was more compressed at 1.5 MPa of the second cycle (−237 µm) than at 1.5 MPa of the first cycle (−180 µm). Although the electrical short circuit must have already formed at the end of the first cycle (the CV at 1.5 MPa of the first cycle clearly shows some tilting and it can also be seen in the oxygen-operated impedance spectrum that the curve is smaller), it vanished when the contact pressure was reduced again to 0.2 MPa. But at the end of the second contact pressure cycle the electrical short circuit is stronger and the following contact pressure reduction does not lead to a complete disappearance of that circuit any more. The reason for that stronger short circuit is obviously the additional MEA compression which happens during the second cycle. A possible cause for this additional thickness loss is given further down in this chapter.

Another contact pressure cycling experiment with another BASF–MEA in the serpentine flow field (not shown here) showed the same thickness loss behavior as the MEA in the grid flow field, which means the MEA

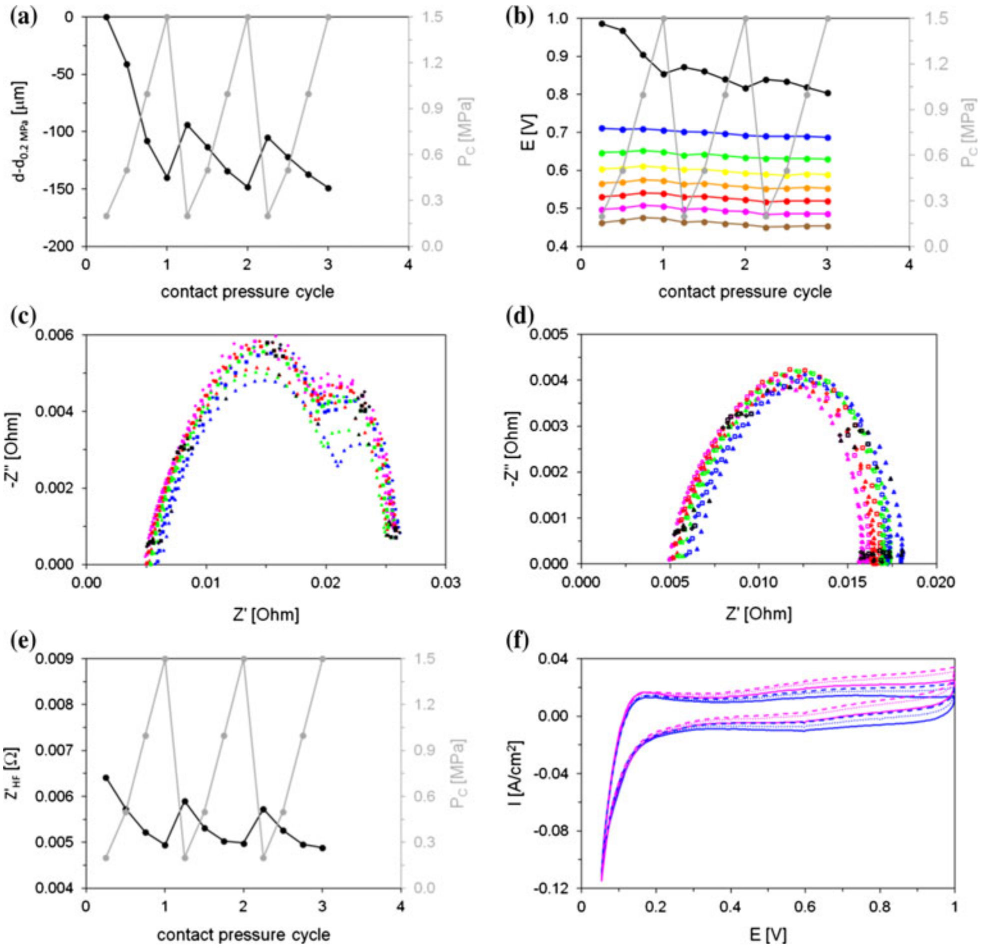

Fig. 20 MEA thickness changes (**a**), selected points of IV-curve (**b**), EIS-spectrum at 0.3 A/cm^2 with air (**c**) and oxygen (**d**), high-frequency resistance at 0.3 A/cm^2 (**e**), and cyclic voltammetry (**f**) as function of contact pressure cycling of BASF–MEA at 160 °C, 1 atm, *grid flow field* with H$_2$/air ($\lambda = 1.2/2$) [**b**, **c**, **e**], H$_2$/O$_2$ ($\lambda = 1.2/9.5$) [**d**], and with H$_2$/N$_2$ [**f** 0.1/>0.1 L/min] (**b** *j* in A/cm^2: *black* 0, *dark blue* 0.1, *green* 0.2, *yellow* 0.3, *orange* 0.4, *red* 0.5, *purple* 0.6, *brown* 0.7, **c**, **d**, **f** P_C in MPa: *blue* 0.2, *green* 0.5, *red* 1, *purple* 1.5, **c**, **d** contact pressure cycle: *black triangles* first, *black squares* second, *black diamonds* third, **f** contact pressure cycle: *continuous lines* first, *dotted lines* second, *dashed lines* third). (Color figure online)

thickness value at the highest applied contact pressure (1.5 MPa) is similar for all three contact pressure cycles. It could be a quality issue that plays a role here, because a fully automated MEA production process does not exist yet so that inherent differences between the MEAs cannot be excluded. For the MEA in the grid flow field the CV tilting gets more pronounced from cycle to cycle. Thus, an increase in electrical short circuit with increasing contact pressure cycle takes place although the maximum applied contact pressure was not raised and a further MEA thickness loss could also not be observed. If one again assumes GDL penetration into the membrane as cause for the electrical short circuit formation, then the short circuit current increase from cycle to cycle means that the damage of the first over-compression facilitates further defects (autocatalysis).

From the impedance spectrum in air-operating mode, it can be seen for the MEA in the serpentine flow field (Fig. 19c) that the mass transport limitation loop strongly decreases from 0.2 to 0.5 MPa, but this decrease slows down and stabilizes when the contact pressure is increased from 0.5 over 1 to 1.5 MPa. (The curve at 1.5 MPa is hard to analyze because a slight increase in the catalytic loop has taken place at the same time which then stays constant for all subsequent contact pressures.) Certainly, one reason for this mass transport improvement with increasing contact pressure is that the diffusion path length for the reactant gases from the flow field channels to the catalyst sites has shortened because the GDL thickness has strongly decreased due to compression. The weakening of the mass transport limitation at higher contact pressures may be attributed to GDL intrusion into the flow field channels so that reactant flow field pressure drop is increasing. But it cannot be that strong so that the effect of diffusion path length reduction still prevails. The first contact pressure reduction to 0.2 MPa leads to higher mass transport limitation again, even though it is less pronounced compared to the curve of the first cycle. The reason is that the GDL remains in an increasing compressed state due to elasticity loss and, therefore, the diffusion path length also remains shorter. According to the thickness curve (MEA thickness loss curve should be dominated by GDL behavior), the mass transport limitation loop at 0.2 MPa of the second cycle was expected to be located between the curves at 0.5 and 1 MPa of the first cycle. It was mentioned by Nitta [12] that a large GDL strain behavior at low contact pressures is most probably due to the smoothening of the rough surface of the GDL which is easily imaginable for a woven GDL structure like in BASF–MEAs. Therefore, the thickness curve of the first contact pressure cycle is not applicable for thickness comparisons, at least not the lower contact pressures values. A comparison of the mass transport limitation loops at 0.5 MPa of the second and 1.5 MPa of the first cycle shows that the curve at 0.5 MPa is somewhat bigger, in spite of almost the same thickness value. An even larger mass transport limitation loop can be observed at 0.2 MPa of the third cycle, although it also possesses the same thickness. There obviously is a further effect which irreversibly influences the mass transport limitation behavior and which depends on contact pressure but does not show in the thickness curve. It is imaginable that the porous structure of the MPL might be affected by partial destruction. The MPL is quite thin and its compressibility should not be as high as for the GDL so that MPL-related thickness changes cannot be detected.

The impedance spectrum in air-operating mode for the strongly compressed MEA in the grid flow field (Fig. 20c) shows that a severe increase in mass transport limitation must take place when increasing the contact pressure from 0.2 to 1.5 MPa for the first time. The negative impact on reactant gas supply is much higher right from the beginning than the effect of a shorter diffusion path length. When decreasing the contact pressure, the mass transport limitation loop only partially recovers. All signs indicate that MPL pore destruction partially takes place. The reversible part must come from pores which were squeezed but not destroyed by the previous compression. These pores can expand again and, therefore, the reactant gas supply improves. During the second contact pressure cycle, the mass transport limitation loop is re-increasing and reaches the same value at 1.5 MPa as in the first cycle. In contrast to the MEA in the serpentine flow field, almost no further thickness loss occurs during the second contact pressure cycle for this MEA. Therefore, almost no additional stress on the MPL should have occurred. That is why the mass transport limitation loop at 0.2 MPa of the third cycle does not differ much from the one at 0.2 MPa of the previous cycle.

Contact resistances (BPP/GDL and GDL/CL) have a strong impact on HFR in the contact pressure range used for the cycling experiment. The question is whether the impact of these contact resistances on the total HFR can be separated with the help of the contact pressure cycling experiments. It is assumed as a first step that similar GDL thickness values mean a similar GDL deformation behavior into the flow field channels and, concomitantly, a similar contact area between BPP and GDL and, therefore, a similar contact resistance at this interface. It can be seen for the MEA in the grid flow field (Fig. 20) that, after the first contact pressure reduction, the GDL thickness is located a little bit above the thickness value for 1 MPa of the first cycle, but the HFR at 0.2 MPa of the second cycle is much higher. It is in the same range as for 0.5 MPa of the first cycle, and by far not for 1 MPa. According to this, more than half of the HFR increase after the first contact pressure reduction must be attributed to the GDL/CL contact resistance. It can additionally be concluded from the similar HFR values for 0.2 MPa of the second and 0.5 MPa of the first cycle that the BPP/GDL contact resistance could not have changed much when the contact pressure was increased from 0.5 to (almost) 1 MPa in the first cycle. That means, although the MEA thickness strongly decreased in this contact pressure range, there cannot be an effect on BPP/GDL contact resistance. The initial deformation behavior is obviously so strong for this MEA and, therefore, the contact gets so good, that the BPP/GDL contact resistance is apparently no longer affected after the first application of 0.5 MPa. Thus, all HFR changes during the cycling experiments after that point can be solely attributed to the GDL/CL contact resistance. It can be seen that the GDL/CL contact resistances are the same for the second and third contact pressure cycle. There is no reason why the reversible GDL/CL behavior should have changed between the first and second cycle. From this it follows that the irreversible HFR improvement after the first contact pressure reduction must be attributed to the BPP/GDL contact resistance. In summary, for this MEA type in combination with this flow field geometry, the contact resistance at the interface GDL/CL is obviously much more important at higher contact pressures than the BPP/GDL contact resistance. The latter only plays a role for the lowest contact pressure.

For the MEA in the serpentine flow field (Fig. 19), both contact resistances (BPP/GDL and GDL/CL) must be reversible for the first contact pressure reduction. The reversible BPP/GDL contact resistance means that the GDL is still flexible enough after being exposed to 1.5 MPa for the first time that it can completely withdraw from the flow field channels when the first contact pressure reduction takes place. This does not happen for the second contact pressure reduction. It was already mentioned before that the MEA is more compressed at the end of the second cycle than after the first cycle. It is supposed that this additional thickness loss is caused by crushing of some GDL regions which could withstand the applied compressive pressure for the first time, but not the repeated exposure to the higher contact pressures. This additional deformation behavior happens between 0.5 and 1 MPa during the second cycle. It can be seen that the HFR at 1 MPa is slightly improved when compared to the value of the first cycle, while virtually no HFR change can be observed for 1.5 MPa. That means the contribution of the contact resistance at the BPP/GDL interface to the total HFR is negligible at the higher contact pressures. But the additional deformation does have an effect for the lowest contact pressure as the reduced HFR value at 0.2 MPa after the second contact pressure reduction clearly shows. The value at 0.5 MPa is also slightly affected. The GDL intrusion into the flow field channels is obviously not fully reversible anymore which leads to an enhanced contact area and, therefore, to a reduced contact resistance between BPP and GDL.

If one compares the absolute HFR values between the two MEAs under consideration of the real contact pressure (nominal contact pressures were used for the pictures), it can be noticed that they do not differ much for nominal contact pressures equal or slightly higher 0.5 MPa, from whereon the BPP/GDL contact resistance is negligible. That means the GDL/CL contact resistance is only a function of contact pressure and does not depend on the GDL deformation behavior (which is different for the two MEAs). The contact resistance at the BPP/GDL interface is only important for the lowest contact pressures. For the MEA in the grid flow field, the impact of the BPP/GDL contact resistance is not negligible for the very first measurement at 0.2 MPa. Here, both kinds of contact resistances must have been of the same size. For the MEA in the serpentine flow field, all measurements at 0.2 MPa (0.5 MPa) must be strongly (still slightly) affected by the BPP/GDL contact resistance. This different behavior is caused by the different deformation behavior of the MEAs inside the respective flow field type.

If a regression line is fitted to the linear curve part in Fig. 2 for the BASF–MEAs and extended to a real contact pressure of 1.5 MPa, then the contribution of GDL/CL contact resistance on total resistance can be quantified. It turns out that GDL/CL magnitude of percentage is about 6 % for both the flow field types at a real contact pressure of 1.5 MPa. A real contact pressure of 1.5 MPa is quite at the low end of normally applied contact pressures. Consequently, the impact of membrane resistance on the total resistance is by far the most important one.

If the results from the BASF–MEA contact pressure cycling experiments could be transferred to DPS–MEA as well as FuMA-Tech–MEA and membrane regression line procedure is applied, then the contribution of the GDL/CL interface resistance on total resistance at a real contact pressure of 1.5 MPa would also be 6 % for DPS–MEA and 14 % for FuMA-Tech–MEA, respectively.

4 Conclusions

In the first part of the paper, PBI-based MEAs from different suppliers (BASF, FuMA-Tech, and DPS) were thoroughly evaluated by fuel cell testing and μ-CT images with regard to compression behavior.

(1) It could be shown that proposed membrane thickness loss due to MEA compression proved to be much less than expected or it was even non-existing. When membrane thickness loss was taking place at all, it was only registered at higher contact pressures and then to a marginal amount. Thus, GDL thickness loss was the main source for the observed total MEA thickness loss.
(2) GDL thickness loss was different for the three MEA types. The differences could be attributed to varying GDL material types utilized (carbon cloth vs. carbon paper for BASF vs. DPS). Additionally, even when the same basic type was used (carbon paper for DPS and FuMA-Tech), the measured data revealed that materials with completely different material properties (e.g., thickness) must have been used.
(3) It was shown by the application of two different flow field types (grid and serpentine) that GDL compressibility behavior and, therefore, fuel cell performance properties strongly depended on flow field geometry. GDL deformation behavior had a big impact on the HFR and on mass transport limitation behavior.
(4) It could be seen from μ-CT images and MEA thickness loss curve that GDL compressive strain is large at low compressive stress due to strong compressibility. The higher the compressive stress got, the less compressive strain could be observed.
(5) Irreversible mechanical damages were proposed through electrochemical data interpretation and were attributed to the physical destruction of the GDL structure and over-compression, for this work in case of the BASF–MEA. The evaluation of the electrochemical data led to the conclusion that physical damages like GDL fiber penetration must have been the reason for electrical short circuit formation and also for hydrogen crossover elevation because of pinhole formation. These physical damages could in detail be visualized through μ-CT and SEM imaging where fibers of the GDL penetrated at first the MPL and then the membrane.

The second major part of the paper was devoted to contact pressure cycling experiments to evaluate whether MEAs are permanently impacted by compressive forces, and if that is the case, whether it is possible to identify and distinguish reversible and irreversible effects of compression on MEAs. Only BASF–MEAs in combination with the two flow field types were investigated.

(1) It was shown that elasticity loss of the GDL material had occurred which could be attributed to the irreversible destruction of porous GDL regions.
(2) Careful investigation led to the conclusion that the effects of compression on the boundary interfaces

between BPP/GDL and GDL/CL, respectively, could be identified for each flow field. It was shown that the BPP/GDL interface resistance was only significant in the lowest contact pressure range where MEA deformation behavior was more pronounced. The GDL/CL interface resistance did not depend on the GDL deformation behavior but was only a function of contact pressure (logarithmically decreasing with increasing contact pressure).

(3) For medium and higher contact pressures, the contribution of the contact resistances on total HFR was low against membrane resistance contribution.

Acknowledgments The authors would like to thank Nadine Bruns and Stefanie Laue who did an excellent job in the laboratories to gather the data for this publication. We would also like to thank the European Commission as some of this work was supported by the Seventh Framework Program through the project DEMMEA (Grant Agreement Number 245156).

References

1. Schmidt TJ (2006) Durability and degradation in high-temperature polymer electrolyte fuel cells. ECS Trans 1(8):19–31
2. Tang H, Qi Z, Ramani M, Elter JF (2006) PEM fuel cell cathode carbon corrosion due to the formation of air/fuel boundary at the anode. J Power Sources 158(2):1306–1312
3. Cai M, Ruthkosky MS, Merzougui B, Swathirajan S, Balogh MP, Oh SH (2006) Investigation of thermal and electrochemical degradation of fuel cell catalysts. J Power Sources 160(2): 977–986
4. Wu J, Yuan X-Z, Martin JJ, Wang H, Yang D, Qiao J, Ma J (2010) Proton exchange membrane fuel cell degradation under close to open-circuit conditions. J Power Sources 195(4): 1171–1176
5. LaConti AB, Hamdan M, McDonald RC (2003) Mechanisms of membrane degradation. In: Vielstich W, Gasteiger HA, Lamm A (eds) Handbook of fuel cells—fundamentals, technology and applications, vol 3. Wiley, New York, pp 647–662
6. Borup R, Meyers J, Pivovar B, Kim YS, Mukundan R, Garland N, Myers D, Wilson M, Garzon F, Wood D, Zelenay P, More K, Stroh K, Zawodzinski T, Boncella J, McGrath JE, Inaba M, Miyatake K, Hori M, Ota K, Ogumi Z, Miyata S, Nishikata A, Siroma Z, Uchimoto Y, Yasuda K, Kimijima K-i, Iwashita N (2007) Scientific aspects of polymer electrolyte fuel cell durability and degradation. Chem Rev 107(10):3904–3951
7. Diedrichs A, Wagner P (2012) Performance analysis of a high-temperature polymer electrolyte membrane fuel cell under mechanical compression control. ECS Trans 50(2):1137–1153
8. Lobato J, Canizares P, Rodrigo MA, Pinar FJ, Ubeda D (2011) Study of flow channel geometry using current distribution measurement in a high temperature polymer electrolyte membrane fuel cell. J Power Sources 196(9):4209–4217. doi:10.1016/j.jpowsour.2010.10.017
9. de Bruijn F (2005) The current status of fuel cell technology for mobile and stationary applications. Green Chem 7(3):132–150
10. Zhang H, Zhai Y, Liu G, Hu J, Yi B (2007) Degradation study on MEA in H_3PO_3/PBI high-temperature PEMFC life test. J Electrochem Soc 154(1):B72–B76
11. Chang WR, Hwang JJ, Weng FB, Chan SH (2007) Effect of clamping pressure on the performance of a PEM fuel cell. J Power Sources 166:149–154
12. Nitta I (2008) Inhomogeneous compression of PEMFC gas diffusion layers. Dissertation, University of Technology, Helsinki
13. Lee W, Ho C-H, Van Zee JW, Murthy M (1999) The effects of compression and gas diffusion layers on the performance of a PEM fuel cell. J Power Sources 84:45–51
14. Ge J, Higier A, Liu H (2006) Effect of gas diffusion layer compression on PEM fuel cell performance. J Power Sources 159(2):922–927
15. Kleemann J, Finsterwalder F, Tillmetz W (2009) Characterisation of mechanical behaviour and coupled electrical properties of polymer electrolyte membrane fuel cell gas diffusion layers. J Power Sources 190(1):92–102. doi:10.1016/j.jpowsour.2008.09.026
16. Bandlamudi (2011) Systematic characterization of HT PEMFCs containing PBI/H_3PO_4 systems. thermodynamic analysis and experimental investigations. PhD, Universität Duisburg-Essen, Duisburg-Essen
17. Runte M (2012) Untersuchung des Einflusses verschiedener Anpressdrücke auf Hochtemperatur Polymerelektrolytmembranbrennstoffzellen mittels μ-Computertomographie. (Investigation of the influence of various compression forces on high temperature polymer electrolyte membrane fuel cells by microcomputed tomography). Bachelor, Fachhochschule Münster, NEXT ENERGY EWE-Forschungszentrum für Energietechnologie e.V., Münster, Oldenburg
18. Arlt T (2012) Methodische Untersuchung von Alterungseffekten an Brennstoffzellen mittels Synchrotronradiografie und -tomografie. (Methodic investigation of degradation effects of fuel cells by synchrotron radiography and -tomography). PhD, Technische Universität Berlin, Berlin
19. Schmidt TJ, Baurmeister J (2006) Durability and reliability in high-temperature reformed hydrogen PEFCs. Proton exchange membrane fuel cells. ECS Trans 3(1):861–869
20. BASF Celtec® MEAs Inc. Membrane electrode assemblies for high temperature PEM fuel cells, data sheet provided by BASF
21. James JP (2012) Micro-computed tomography reconstruction and analysis of the porous transport layer in polymer electrolyte membrane fuel cells. Master, Queen's University, Kingston
22. Karwey M (2012) Untersuchung der mechanischen Belastung von Brennstoffzellenmembranen in Testzellen durch auftretenden Anpressdruck. (Investigation of the mechanical stress on fuel cell membranes by compression). Bachelor, Fachhochschule Südwestfalen
23. Cooper KR (2008) In situ PEMFC fuel crossover and electrical short circuit measurement. Fuel Cell Mag Aug/Sep
24. Le Bihan D, Brasser PJ (1995) Molecular diffusion and nuclear magnetic resonance. In: Le Bihan D (ed) Diffusion and perfusion magnetic resonance imaging. Raven Press, Ltd., New York, pp 5–17
25. Mathias MF, Roth J, Fleming J, Lehnert W (2003) Diffusion media materials and characterisation. In: Vielstich W, Gasteiger HA, Lamm A (eds) Handbook of fuel cells—fundamentals, technology and application, vol 3. Wiley, New York, pp 517–537
26. Schneider IA, Kramer D, Wokaun A, Scherer GG (2007) Effect of inert gas flow on hydrogen underpotential deposition measurements in polymer electrolyte fuel cells. Electrochem Commun 9(7):1607–1612